Quantum Coherence in Photosynthetic Light Harvesting

Akihito Ishizaki[1,2] and Graham R. Fleming[1,2]

[1]Department of Chemistry, University of California, Berkeley, California 94720

[2]Physical Biosciences Division, Lawrence Berkeley National Laboratory, Berkeley, California 94720

Annu. Rev. Condens. Matter Phys. 2012. 3:333–61

First published online as a Review in Advance on December 13, 2011

The *Annual Review of Condensed Matter Physics* is online at conmatphys.annualreviews.org

This article's doi:
10.1146/annurev-conmatphys-020911-125126

1947-5454/12/0310-0333$20.00

Keywords

electronic energy transfer, pigment-protein complexes, two-dimensional electronic spectroscopy, non-Markovian interplay between electronic excitation and its protein environment

Abstract

Recent two-dimensional (2D) electronic spectroscopic experiments revealed that electronic energy transfer in photosynthetic light harvesting involves long-lived quantum coherence among electronic excitations of pigments. These findings have led to the suggestion that quantum coherence might play a role in achieving the remarkable quantum efficiency of photosynthetic light harvesting. Further, this speculation has led to much effort being devoted to elucidation of the quantum mechanisms of the photosynthetic excitation energy transfer (EET). In this review, we provide an overview of recent experimental and theoretical investigations of photosynthetic electronic energy transfer, specifically addressing underlying mechanisms of the observed long-lived coherence and its potential roles in photosynthetic light harvesting. We close with some thoughts on directions for future developments in this area.

1. INTRODUCTION

Photosynthesis is the natural process of harvesting, converting, and storing the energy of sunlight. With minor possible exceptions near hydrothermal vents, deep in the dark of the ocean floor, this process provides the energy source for essentially all living things on Earth. Photosynthetic conversion of the energy of sunlight into its chemical form suitable for cellular processes involves a variety of physicochemical mechanisms (1). The conversion starts with the absorption of a photon of sunlight by one of the light-harvesting pigments, followed by transfer of electronic excitation energy to the reaction center (RC). There the excitation energy initiates an electron transfer process to build up a chemical potential that fuels chemical reactions producing energy-rich complex carbohydrates. At low light intensities, the quantum efficiency of the transfer is near unity; that is, each of the absorbed photons almost certainly reaches the RC and drives the electron transfer reactions. A longstanding question in photosynthesis has been the following: How do light-harvesting systems deliver such high efficiency in the presence of disordered and fluctuating dissipative environments? At high light intensities, however, the RC is protected by regulation mechanisms that lead to quenching of excess excitation energy in light-harvesting proteins to mitigate oxidative damage (1, 2). The precise molecular mechanisms of these initial stages of photosynthesis are not yet fully elucidated from the standpoint of physical sciences.

The observation of long-lived electronic quantum coherence in a light-harvesting protein [the Fenna-Matthews-Olson (FMO) complex (1, 3)] by Fleming and coworkers (4–6) stimulated a huge burst of activity among theorists and experimentalists (7–40). Much of the interest arose because the finding of electronic quantum coherence in a "warm, wet, and noisy" biological system was surprising. The initial experiments were carried out at 77 K, but more recent studies by two groups have detected coherence lasting at least 300 fs at physiological temperatures (41, 42). In addition, extensive quantum coherence was observed in the most important light-harvesting complex on Earth, the light-harvesting complex II, or LHCII (43).

In this review, we illustrate the present state of understanding of electronic quantum coherence in photosynthetic light harvesting with the aim of shedding light on the physical mechanisms underlying the long-lived coherence and the potential functions such coherence could facilitate. Recent reviews have focused on the theoretical and experimental details (44, 45), and we refer the readers to these articles for greater detail. We conclude with some thoughts as to future directions for research in this area.

2. MODELING LIGHT-HARVESTING SYSTEMS

We begin by describing the electronic states of the pigment-protein complexes (PPCs). Consider a PPC consisting of N pigments. To describe excitation energy transfer (EET), we restrict the electronic spectra of mth pigment in a PPC to the ground state $|\varphi_{mg}\rangle$ and the first excited state $|\varphi_{me}\rangle$. When the mth and nth pigments are situated in close proximity and the mth pigment is excited, the excitation energy may be transferred to the nth pigment. We assume that there is no orbital overlap between the two molecules so that electrons can be assigned unambiguously to one molecule or the other. In this situation the PPC Hamiltonian for describing photosynthetic EET can be expressed as (46)

$$H_{\mathrm{PPC}} = \sum_{m=1}^{N} \sum_{a=\mathrm{g,e}} H_{ma}(\mathbf{x}) \,|\, \varphi_{ma}\rangle\langle\varphi_{ma} \,| + \sum_{m,n} \hbar J_{mn} \,|\, \varphi_{me}\rangle\langle\varphi_{mg} \,|\otimes|\, \varphi_{ng}\rangle\langle\varphi_{ne} \,|. \qquad 1.$$

Here, $H_{ma}(\mathbf{x}) = \epsilon_{ma}(\mathbf{x})$ + (nuclear kinetic energy) (a = g, e) is the Hamiltonian describing the nuclear dynamics associated with an electronic state $|\varphi_{ma}\rangle$, where $\epsilon_{ma}(\mathbf{x})$ is the potential energy as a function of the set of the relevant nuclear coordinates including protein degrees of freedom (DOFs), $\mathbf{x}$. The electronic coupling J_{mn} is also influenced by the nuclear motions and local polarizations of the protein environment (46–48). However, we assume that nuclear dependence of J_{mn} is vanishingly small as usual.

The normal mode treatment is usually assumed for the PPC nuclear dynamics, because anharmonic motion with large amplitudes and long timescales produces static disorder on timescales irrelevant to photosynthetic EET (44, 49, 50). Furthermore, it may be assumed that nuclear configurations for the electronic excited states of pigments are not greatly different from those for the ground states owing to the absence of large permanent dipoles on the pigments. Thus, $H_{mg}(\mathbf{x})$ and $H_{me}(\mathbf{x})$ can be modeled as a set of displaced harmonic oscillators,

$$H_{mg}(\mathbf{x}) = \epsilon_{mg}(\mathbf{x}^0_{mg}) + \sum_{\xi} \frac{\hbar\omega_{m\xi}}{2}(p^2_{m\xi} + q^2_{m\xi}), \qquad 2.$$

and

$$H_{me}(\mathbf{x}) = H_{mg}(\mathbf{x}) + \hbar\Omega_m - \sum_{\xi} \hbar\omega_{m\xi} d_{m\xi} q_{m\xi}, \qquad 3.$$

where $\mathbf{x}^0_{mg}$ is the equilibrium configuration of the nuclear coordinates associated with the electronic ground state of the mth pigment, and $q_{m\xi}$ is the dimensionless normal mode coordinate with accompanying frequency $\omega_{m\xi}$ and momentum $p_{m\xi}$. $d_{m\xi}$ is the dimensionless displacement. For later convenience, we set $\epsilon_{mg}(\mathbf{x}^0_{mg}) = 0$ without loss of generality. The Franck-Condon transition energy, $\hbar\Omega_m = \epsilon_{me}(\mathbf{x}^0_{mg}) - \epsilon_{mg}(\mathbf{x}^0_{mg})$, is also termed the site energy in the literature. After electronic excitation in accordance with the vertical Franck-Condon transition, reorganization takes place from the nuclear configuration $\mathbf{x}^0_{mg}$ to the actual equilibrium configuration in the excited state $\mathbf{x}^0_{me}$ with dissipating reorganization energy defined as $\hbar\lambda_m = \epsilon_{me}(\mathbf{x}^0_{mg}) - \epsilon_{me}(\mathbf{x}^0_{me})$. This reorganization proceeds on a finite timescale, τ^{rxn}_m (**Figure 1**).

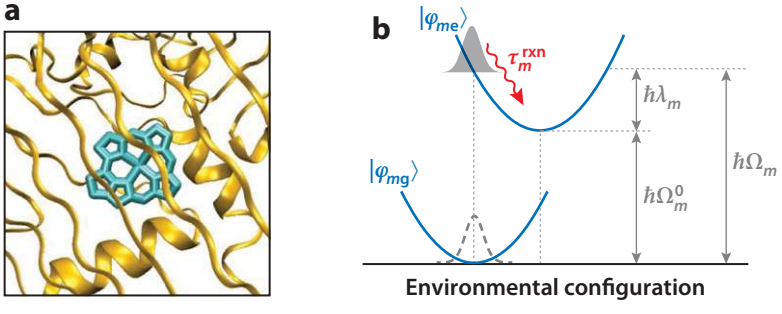

Figure 1

Schematic illustration of the mth pigment embedded in a protein (a) and the electronic ground and excited states of the mth pigment, $|\varphi_{mg}\rangle$ and $|\varphi_{me}\rangle$, affected by nuclear motion of the protein environment (b). After electronic excitation in accordance with the vertical Franck-Condon transition, reorganization takes place from the equilibrium nuclear configuration with respect to the electronic ground state $|\varphi_{mg}\rangle$ to the actual equilibrium configuration in the excited state $|\varphi_{me}\rangle$ with dissipation of the reorganization energy, $\hbar\lambda_m$. This reorganization proceeds on a characteristic timescale, τ^{rxn}_m.

From the dynamical point of view, Equation 1 demonstrates that the electronic energies of the pigments experience dynamic modulations caused by the environmental motion, e.g., the intramolecular nuclear motion and the surrounding protein motion. Due to a huge number of the environmental DOFs, such modulations can be modeled as random fluctuations. To describe the modulations we introduce the collective energy gap coordinate (49),

$$u_m = H_{me}(\mathbf{x}) - H_{mg}(\mathbf{x}) - \hbar\Omega_m. \quad 4.$$

Because $\{q_\xi\}$ are normal mode coordinates, $u_m(t) \equiv e^{iH_{mg}t/\hbar} u_m e^{-iH_{mg}t/\hbar}$ yields a Gaussian process, and hence all the environment-induced processes can be quantified by two-point correlation functions of $u_m(t)$. Fluctuations in the electronic energy of the mth pigment are described by the symmetrized correlation function as $S_m(t) = (1/2)\langle\{u_m(t),u_m(0)\}\rangle_{mg}$, where $\langle\ldots\rangle_{mg}$ denotes averaging over $\rho_{mg}^{eq} = e^{-\beta H_{mg}}/\mathrm{Tr}[e^{-\beta H_{mg}}]$, with β being inverse temperature. In addition, environmental reorganization involving the dissipation of reorganization energy is characterized by the response function, $\chi_m(t) = (i/\hbar)\langle[u_m(t), u_m(0)]\rangle_{mg}$. In the classical limit the symmetrized correlation and response functions are simply expressed by the relaxation function $\Gamma_m(t)$ via the classical fluctuation-dissipation relation (FDR) (51),

$$\beta S_m(t) \simeq \Gamma_m(t), \quad \chi_m(t) = -\frac{d}{dt}\Gamma_m(t), \quad 5.$$

where the Stokes shift magnitude is expressed as $\Gamma_m(0) = 2\hbar\lambda_m$ (49, 52).

3. INHERENT NON-MARKOVIAN ASPECTS OF ELECTRONIC ENERGY TRANSFER

The electronic coupling $\hbar J_{mn}$ between pigments and the excitation-environment coupling characterized by the reorganization energy $\hbar\lambda_m$ are two fundamental interaction mechanisms determining the nature of EET in photosynthetic PPCs. The transfer processes are usually described in one of two perturbative limits. When the electronic coupling $\hbar J_{mn}$ is small in comparison with the excitation-environment coupling $\hbar\lambda_m$, the interpigment electronic coupling can be treated perturbatively. This treatment yields Förster theory (53). In the opposite limit, when the electron-nuclear coupling is small, it is possible to treat the electron-nuclear coupling perturbatively to obtain a quantum master equation. However, a key quantity in EET is the relation between two timescales (46): the characteristic timescale of the environmental reorganization, τ_m^{rxn}, and the inverse of the electronic coupling, J_{mn}^{-1}, which is the time the excitation needs to move from one pigment to another neglecting any additional perturbations.

3.1. Förster Theory

In the case of $\tau_m^{rxn} \ll J_{mn}^{-1}$, it is impossible to construct a wave function straddling multiple pigments. The nuclear reorganization introduces fast dephasing, and hence EET occurs after the nuclear equilibration associated with the excited pigment. In this situation, EET is described as a diffusive motion similar to classical random walk; it follows classical rate laws where the transition rate is given by Förster theory (53). Although Förster theory is not capable of describing quantum coherent EET, it is instructive regarding the non-Markovian interplay between electronic excitation and its associated environmental DOFs, i.e., the nature of spectral linebroadening caused by electronic energy fluctuations and site-dependent reorganization dynamics involving dissipation of reorganization energies, which play a

crucial role in exploring appropriate theories of quantum coherent EET in photosynthetic PPCs (15, 16, 44).

Förster derived the EET rate expression with a second-order perturbative treatment of the electronic coupling between the pigments (53). The resultant rate from $|m\rangle \equiv |\varphi_{me}\rangle\prod_{k(\neq m)}|\varphi_{kg}\rangle$ to $|n\rangle \equiv |\varphi_{ne}\rangle\prod_{k(\neq n)}|\varphi_{kg}\rangle$ is expressed as the overlap integral between the fluorescence spectrum of a donor $F_m[\omega]$ and the absorption spectrum of an acceptor $A_m[\omega]$ as

$$k_{m\leftarrow n} = J_{mn}^2 \int_{-\infty}^{\infty} \frac{d\omega}{2\pi} A_m[\omega] F_n[\omega]. \quad 6.$$

From the viewpoint of electronic energy fluctuations, the overlap integral in Equation 6 is understood as fluctuation-induced resonance. As discussed in Section 2, electronic states and energies of the pigments experience fluctuations induced by the environment. At the instant that the fluctuations bring the energy gap between the donor's electronic ground and excited states, and that of the acceptor, into resonance, electronic excitation tunnels from the donor to the acceptor with conservation of energy. Recently, this kind of environment-controlled mechanism has attracted attention from the standpoint of quantum physics, e.g., environment-assisted or dephasing-assisted quantum transport (11, 12, 27, 28, 35).

In terms of dissipation of reorganization energies, the Förster rate expression implies the following: (*a*) First, the reorganization of the initial state $|m\rangle = |\varphi_{me}\rangle\prod_{k(\neq m)}|\varphi_{kg}\rangle$ takes place instantaneously. (*b*) Subsequently, the electronic de-excitation of the *n*th pigment and the excitation of the *m*th pigment occur from the equilibrium environmental DOFs of the initial state to the nonequilibrium environmental DOFs or hot phonons of the final state $|n\rangle = |\varphi_{ne}\rangle\prod_{k(\neq n)}|\varphi_{kg}\rangle$, in accordance to the Franck-Condon principle. (*c*) Finally, the reorganization of the final state follows. These sequential processes involving the site-dependent reorganization dynamics are the key assumptions of Förster theory. Extensions of Förster theory also have been explored to treat finite timescales of the reorganization, i.e., the so-called hot transfer mechanism or nonequilibrium effects (54–56).

3.2. Delocalized Exciton States

In the opposite case where $J_{mn}^{-1} \ll \tau_m^{\mathrm{rxn}}$, the excitation can travel almost freely from one pigment to another according to the Schrödinger equation (57–59) until the nuclear configurations are quenched by reorganization. The excitation travels through photosynthetic PPCs as a quantum mechanical wave packet keeping its phase coherence, and thus this process is termed coherent transfer. In this limit, it is convenient to separate the environmental contributions from the PPC Hamiltonian, and thus Equation 1 is recast into

$$H_{\mathrm{PPC}} = H_{\mathrm{ex}} + H_{\mathrm{ex\text{-}env}} + H_{\mathrm{env}}. \quad 7.$$

The first term on the right-hand side is the electronic excitation Hamiltonian comprised of the Franck-Condon energies and electronic couplings,

$$H_{\mathrm{ex}} = \sum_m \hbar\Omega_m B_m^\dagger B_m + \sum_{m,n} \hbar J_{mn} B_m^\dagger B_n, \quad 8.$$

where creation and annihilation operators have been introduced: $B_m^\dagger = |\varphi_{me}\rangle\langle\varphi_{mg}|$ and $B_m = |\varphi_{mg}\rangle\langle\varphi_{me}|$, respectively. The second part in Equation 7 corresponds to the coupling of environmental DOFs to the electronic excitations,

$$H_{\text{ex-env}} = \sum_m u_m B_m^\dagger B_m. \qquad 9.$$

The last term in Equation 7 is a set of normal mode Hamiltonians, i.e., the phonon Hamiltonian expressed as $H_{\text{env}} = \sum_m H_{mg}(\mathbf{x})$. We note that the standard Hamiltonian describing photosynthetic EET (Equations 7–9) is different from the so-called spin-boson model (60), where a two-level system is coupled to a single environment composed of harmonic oscillators. This spin-boson model is usually employed to describe electron transfer reactions in condensed phases (61, 62), not the EET dynamics. A two-state system describing a pair of donor-acceptor pigments in EET is completely different from a two-level system corresponding to electronic ground and excited states, as illustrated in **Figures 1** and **2**. The donor and acceptor in a two-state system are coupled to individual phonon modes, whereas both of the electronic ground and excited states in a two-level system are associated with the same phonon modes.

In general, spectroscopic measurements provide information projected onto energy eigenstates, and therefore it is customary to employ eigenstates of electronic excitation energies, which are termed excitons in the literature. For analyzing spectroscopic data, one usually diagonalizes only the excitation Hamiltonian in Equation 8, yielding the excitation energy eigenstates. Exciton states in the one-excitation manifold are expressed as

$$|e_\mu\rangle = \sum_m c_{\mu m}\Big(|\varphi_{me}\rangle \prod\nolimits_{k(\neq m)} |\varphi_{kg}\rangle\Big), \qquad 10.$$

whereas excitons in the two-excitation manifold are given as

$$|f_{\bar{\nu}}\rangle = \sum_{m,n} c_{\bar{\nu}(m,n)}\Big(|\varphi_{me}\rangle\,|\varphi_{ne}\rangle \prod\nolimits_{k(\neq m,n)} |\varphi_{kg}\rangle\Big). \qquad 11.$$

In this exciton representation, diagonal matrix elements of the excitation-environment coupling Hamiltonian, $\langle e_\mu | H_{\text{ex-env}} | e_\mu\rangle = \sum_m |c_{\mu m}|^2 u_m$, are interpreted as fluctuations in the exciton energies. Off-diagonal elements such as $\langle e_\mu | H_{\text{ex-env}} | e_\nu\rangle = \sum_m c_{\mu m}^* c_{\nu m} u_m$ contribute to transitions from excitons to other excitons within the same manifolds. A transition between

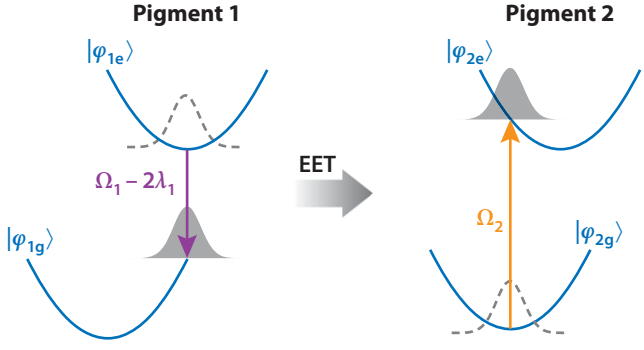

Figure 2

Schematic of the excitation energy transfer (EET) mechanism from pigment 1 to pigment 2 in Förster theory. In Förster theory, the de-excitation (*down-pointing purple arrow*) and excitation (*up-pointing orange arrow*) occur from the equilibrium phonons of the initial state $|1\rangle = |\varphi_{1e}\rangle|\varphi_{2g}\rangle$ to the nonequilibrium phonons of the final state $|2\rangle = |\varphi_{1g}\rangle|\varphi_{2e}\rangle$ in accordance to the vertical Franck-Condon transition.

two excitons requires that they share electronic excitation of the same pigments, i.e., there is spatial overlap between the two excitons. This aspect was visually illustrated with the help of two-dimensional (2D) electronic spectroscopy (4, 63). The most commonly used theory to calculate the transition rates in the literature of photosynthetic EET is Redfield theory (64) or the modified Redfield theory (65, 66). Innovated and established in the field of nuclear magnetic resonance, Redfield theory has been employed in wide areas of condensed phase chemical dynamics such as electron transfer reactions and photosynthetic EET. Although Redfield theory has been broadly applied, its original form is based on the Markov approximation and on the assumption that the system-environment interaction is sufficiently weak that a second-order perturbative truncation should be valid. Although optical spectra provide us with the information projected onto energy eigenstates, this does not necessarily mean that electronic excitations are always in their energy eigenstates. In addition, whether or not EET dynamics is quantum coherent does not depend on the representation we employ to describe the system. Oscillations of off-diagonal elements in the exciton representation simply transform into oscillatory behavior of population dynamics in the site representation. The choice of representation depends on the phenomena of interest and how to measure them.

Hybrid cases of the Förster-type and the delocalized-exciton-type models have been used to describe specific photosynthetic PPCs. For example, when excitation is strongly delocalized within a group of donor and/or acceptor pigments, but hops incoherently from the donor to acceptor excitons, a description based on generalized Förster theory (67–70) or multichromophoric Förster theory (71) is adequate.

3.3. Intermediate Regime Relevant for Photosynthetic Electronic Energy Transfer

Obviously, there exist regimes of EET where the two coupling magnitudes and/or the two timescales are of similar magnitude, i.e., $\lambda_m \sim J_{mn}$ and/or $\tau_m^{\mathrm{rxn}} \sim J_{mn}^{-1}$. In fact, intermediate regimes are typical for photosynthetic EET (63, 72), and therefore they are of considerable interest. From a theoretical point of view, descriptions of these regimes are challenging because the absence of vanishingly small parameters rules out standard perturbative and Markovian approaches. Several investigations have been devoted to the construction of theories for this intermediate regime (13, 14, 16, 21, 73–78). As emphasized in References 16 and 44, a non-Markovian interplay between electronic excitations and their protein environment, i.e., the site-dependent reorganization dynamics with a characteristic timescale discussed in Section 3.1, is a crucial ingredient of an accurate description. This site-dependent reorganization process becomes more significant when the reorganization energies are not small in comparison to the electronic coupling. However, this process cannot be described by the Redfield equation due to the Markov approximation (15). The Markov approximation requires the environmental DOFs to relax to their equilibrium states instantaneously; that is, the environmental DOFs are always in equilibrium even under the excitation-environment coupling.

Addressing this site-dependent reorganization of protein environments, Ishizaki & Fleming (16) demonstrated a theoretical framework to describe EET in PPCs and derived the second-order cumulant time-nonlocal (2C-TNL) quantum master equation. This equation is recast into the conventional Redfield equation under the Markov approximation, whereas it reduces to Förster theory in the weak electronic coupling limit. For numerical calculations, the Drude-Lorentz spectral density (79), which is also termed the overdamped Brownian oscillator model (49), and the hierarchy expansion technique (80–82) were employed. To examine whether the theory is capable of describing the site-dependent reorganization dynamics, Reference 16 calculated dynamic fluorescence Stokes shift by employing a dimer consisting of

three states: $|0\rangle = |\varphi_{1g}\rangle|\varphi_{2g}\rangle$, $|1\rangle = |\varphi_{1e}\rangle|\varphi_{2g}\rangle$, and $|2\rangle = |\varphi_{1g}\rangle|\varphi_{2e}\rangle$. **Figure 3** presents the dynamics of electronic excitation and the accompanying environmental DOFs as the emission spectra from $|\varphi_{1e}\rangle$ and $|\varphi_{2e}\rangle$. For the calculations, the parameters are chosen to be $\Omega_1 - \Omega_2 = 100\ \mathrm{cm}^{-1}$, $J_{12} = 20\ \mathrm{cm}^{-1}$, $\tau_1^{\mathrm{rxn}} = \tau_2^{\mathrm{rxn}} = 100\,\mathrm{fs}(1/\tau_1^{\mathrm{rxn}} = 1/\tau_2^{\mathrm{rxn}} = 53\,\mathrm{cm}^{-1})$, and $\lambda_1 = \lambda_2 = 200\ \mathrm{cm}^{-1}$. The temperature is set to be 150 K to narrow the spectra. **Figure 3*a*** is the emission spectrum from $|\varphi_{1e}\rangle$ as a function of a delay time t after the excitation of pigment 1. Just after the excitation, the maximum value of the emission spectrum is located in the vicinity of the Franck-Condon energy, $\omega = \Omega_1$. The frequency of a maximum peak position decreases with time and reaches $\omega = \Omega_1 - 2\lambda_1$ with almost constant magnitude. This indicates that the environmental reorganization dynamics takes place prior to the EET. This is reasonable because $\tau_1^{\mathrm{rxn}} < J_{12}^{-1}$. **Figure 3*b*** shows the emission spectrum from $|\varphi_{2e}\rangle$. The contour line of the lowest level clearly shows that the emission spectrum emerges from close to $\omega = \Omega_2$ in the short time region. This indicates that the excitation of pigment 2 occurs from the equilibrium environmental DOFs of the electronic ground state $|\varphi_{2g}\rangle$ to the nonequilibrium environmental DOFs of the electronic excited state $|\varphi_{2e}\rangle$, in accordance with the vertical Franck-Condon principle. Because the reorganization process takes place subsequently, we observe the emission spectrum in the vicinity of $\omega = \Omega_2 - 2\lambda_2$ in the long time region. Clearly, **Figure 3** demonstrates the sequential processes discussed in Section 3.1, which are the key assumption of Förster theory. Hence, the 2C-TNL equation is capable of reproducing the Förster rate (16).

Figure 4 presents population dynamics of $|1\rangle = |\varphi_{1e}\rangle|\varphi_{2g}\rangle$ in a dimer calculated by the 2C-TNL equation and the Markovian Redfield equation for various values of the reorganization energy, $\lambda = \lambda_1 = \lambda_2$. For numerical integration of the Redfield equation, we do not employ

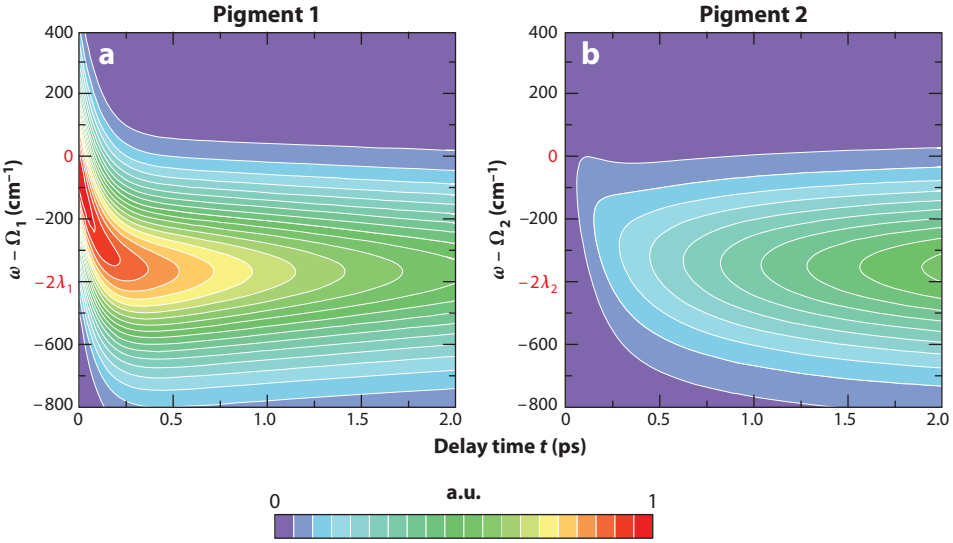

Figure 3

Calculated emission spectra from pigment 1 (*a*) and pigment 2 (*b*) as a function of a delay time t after the photoexcitation of pigment 1. For the calculations, the parameters are chosen to be $\Omega_1 - \Omega_2 = 100\ \mathrm{cm}^{-1}$, $J_{12} = 20\ \mathrm{cm}^{-1}$, $\lambda_1 = \lambda_2 = 200\ \mathrm{cm}^{-1}$, $\tau_1^{\mathrm{rxn}} = \tau_2^{\mathrm{rxn}} = 100\mathrm{fs}$, and $T = 150$ K. The normalization of the spectra is such that the maximum value of panel *a* is unity. Twenty equally spaced contour levels from 0.05 to 1 are drawn. Figure taken from Reference 16.

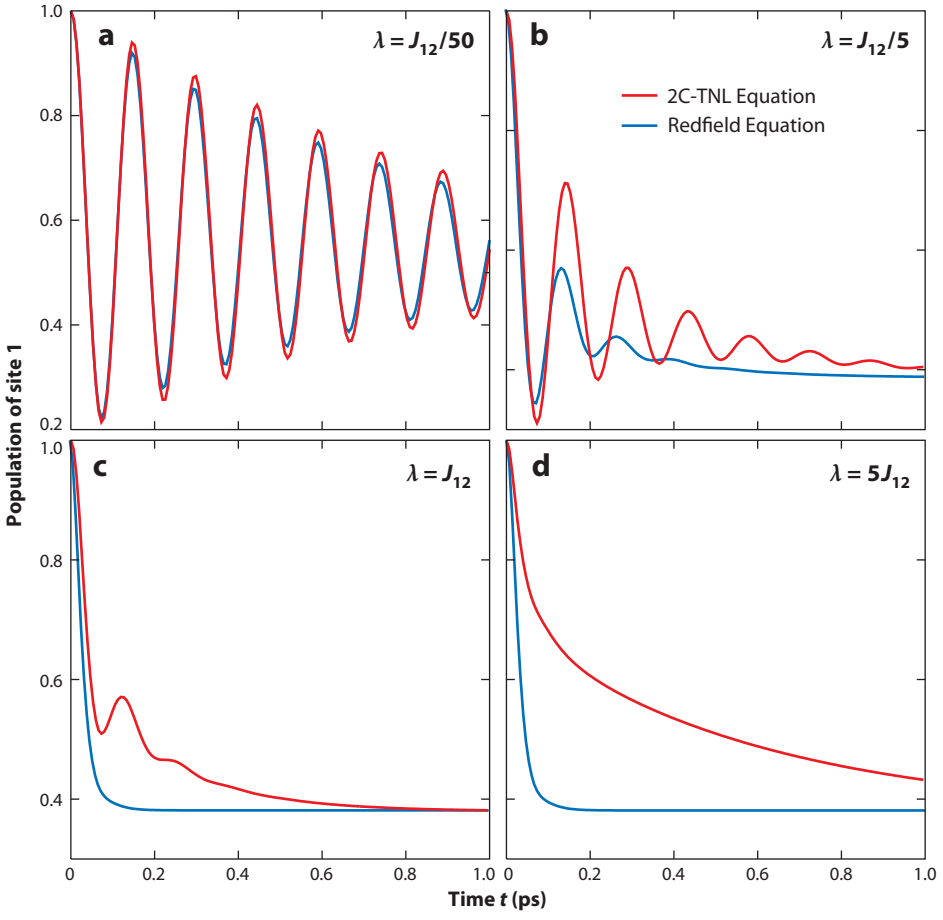

Figure 4

Time evolution of the population of $|1\rangle = |\varphi_{1e}\rangle|\varphi_{2g}\rangle$ in a dimer calculated by the second-order cumulant time-nonlocal (2C-TNL) equation (*red line*) and the Redfield equation in the full form (*blue line*) for various magnitudes of the reorganization energy $\lambda = \lambda_1 = \lambda_2$; (*a*) $\lambda = 2$ cm^{-1}, (*b*) $\lambda = 20$ cm^{-1}, (*c*) $\lambda = 100$ cm^{-1}, and (*d*) $\lambda = 500$ cm^{-1}. The other parameters are fixed to be $\Omega_1 - \Omega_2 = 100$ cm^{-1}, $J_{12} = 100$ cm^{-1}, $\tau_1^{rxn} = \tau_2^{rxn} = 100$ fs, and $T = 300$ K. Figure taken from Reference 16.

any additional approximations such as the secular approximation (46, 64). Although the secular approximation has been widely employed in applications of the Redfield equation, it overestimates the contribution of environment-assisted incoherent EET (15). As the initial condition for calculations, only pigment 1 is assumed to be excited in accordance with the Franck-Condon principle. The other parameters are fixed to be $\Omega_1 - \Omega_2 = 100$ cm^{-1}, $J_{12} = 100$ cm^{-1}, $\tau_1^{rxn} = \tau_2^{rxn} = 100$ fs$(1/\tau_1^{rxn} = 1/\tau_2^{rxn} = 53$ cm$^{-1})$, and temperature 300 K. **Figure 4*a*** is for $\lambda = J_{12}/50$. The dynamics calculated by the two theories are almost coincident with each other. The Markov approximation is appropriate in this case because of the extremely small reorganization energy. **Figure 4*b*** shows the case of $\lambda = J_{12}/5$. The dynamics calculated by the 2C-TNL theory shows long-lasting coherent motion up to 1 ps. However, the dynamics from the Redfield theory dephases on a timescale of less than 400 fs. The cause of the difference is the breakdown of the Markov approximation. The infinitely fast dissipation of reorganization

energy then corresponds to infinitely fast fluctuation according to the FDR. The infinitely fast fluctuation with relatively large amplitude collapses the quantum superposition state. As a result, the coherent motion in the Redfield theory is destroyed rapidly compared with the present theory. **Figure 4*c*** is for the case of $\lambda = J_{12}$. The dynamics calculated from the Redfield theory shows no oscillation; however, the present theory predicts wave-like motion up to 300 fs. **Figure 4*d*** presents the case of $\lambda = 5J_{12}$. The dynamic behavior of the Redfield theory is similar to that in **Figure 4*c*** because the full-Redfield theory predicts λ-independent dynamics for large reorganization energy due to the Markov approximation (16). The dynamics calculated by the 2C-TNL theory also shows no wave-like motion. However, it should be noted that the dynamics involves two timescales. Comparing **Figure 4*d*** with **Figures 4*a*–4*c***, we can recognize that the faster component ($t \lesssim 100$ fs) arises from quantum coherence. The quantum coherent motion is destroyed before the first oscillation, and the subsequent dynamics follows the incoherent motion of the slower component of timescale, which needs thermal activation to overcome an energy barrier between the donor and acceptor. To visualize this statement, it is helpful to consider the following minimal model instead of the PPC Hamiltonian in Equation 1 (16, 44):

$$H_{\mathrm{PPC}} = \sum_{m=0}^{2} \epsilon_m(\mathbf{q}) |\, m\rangle\langle m\,| + \hbar J_{12}(|\,1\rangle\langle 2\,| + |\,2\rangle\langle 1\,|), \qquad 12.$$

where we have introduced $\epsilon_0(\mathbf{q}) = \hbar\omega_{\mathrm{ph}} q_1^2/2 + \hbar\omega_{\mathrm{ph}} q_2^2/2$, and

$$\epsilon_m(\mathbf{q}) = \epsilon_0(\mathbf{q}) + \hbar\Omega_m - \hbar\omega_{\mathrm{ph}} d q_m \quad (m = 1, 2), \qquad 13.$$

with the reorganization energy expressed as $\hbar\lambda_m = \hbar\omega_{\mathrm{ph}} d^2/2$. Equation 12 can be easily diagonalized, and then adiabatic excitonic potential surfaces in the one-excitation manifold can be obtained as

$$E^{\pm}(\mathbf{q}) = \frac{\epsilon_1(\mathbf{q}) + \epsilon_2(\mathbf{q})}{2} \pm \sqrt{\left[\frac{\epsilon_1(\mathbf{q}) - \epsilon_2(\mathbf{q})}{2}\right]^2 + (\hbar J_{12})^2}. \qquad 14.$$

In **Figure 5**, we draw the adiabatic potential surface for the lower energy, $E^{-}(\mathbf{q})$, as a function of two phonon coordinates, q_1 and q_2. The parameters in this model are chosen to be the same as those in **Figure 4*d***. Because the reorganization energy is large compared with the electronic coupling, we can observe two local minima that represent the two sites, $|1\rangle = |\varphi_{1\mathrm{e}}\rangle|\varphi_{2\mathrm{g}}\rangle$ and $|2\rangle = |\varphi_{1\mathrm{g}}\rangle|\varphi_{2\mathrm{e}}\rangle$. Incoherent hopping EET describes the transition between the local minima. Attention is now given to the point of origin, which corresponds to the Franck-Condon state. The energy of the point is higher than the barrier between the minima; therefore, we find that the electronic excited state is delocalized just after the excitation despite being in the incoherent hopping regime, $\lambda > J_{12}$. As time increases, the dissipation of reorganization energy proceeds and the excitation will fall off into one of the minima and become localized. This picture is consistent with **Figure 4*d***. Namely, sluggish dissipation of reorganization energy increases the time an electronic excitation stays above an energy barrier separating pigments and thus prolongs delocalization over the pigments. The dynamic behavior of the intermediate regime (**Figure 4*c***) can be understood as the combined influence of the slow fluctuation effect in the regime of small reorganization energy and

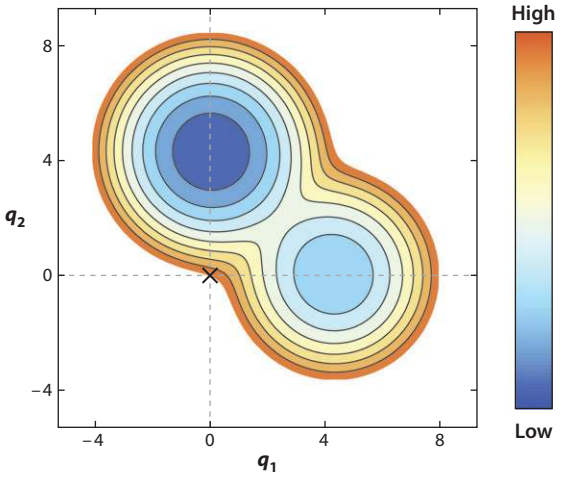

Figure 5

Adiabatic excitonic potential surface $E^{-}(\mathbf{q})$ given by Equation 14. The parameters are chosen to be $\Omega_1 - \Omega_2 = 100\ \text{cm}^{-1}$, $J_{12} = 100\ \text{cm}^{-1}$, $\omega_{\text{ph}} = 53\ \text{cm}^{-1}$, and $\lambda_1 = \lambda_2 = 500\ \text{cm}^{-1}$. Contour lines are drawn at $50\ \text{cm}^{-1}$ intervals. The local minimum located around $(q_1, q_2) = (4,0)$ corresponds to $|1\rangle = |\varphi_{1e}\rangle|\varphi_{2g}\rangle$, whereas that around $(q_1, q_2) = (0,4)$ is $|2\rangle = |\varphi_{1g}\rangle|\varphi_{2e}\rangle$. The point of origin corresponds to the Franck-Condon state.

the slow dissipation effect in the large reorganization energy. Recently, the results presented in **Figure 4** were well reproduced by several theoretical techniques such as the linearized semiclassical initial value representation approach (76), the iterative linearized density matrix propagation scheme (77), the Landmap propagator approach (77), and the quasiadiabatic path-integral scheme (83).

4. TWO-DIMENSIONAL ELECTRONIC SPECTROSCOPY

Dynamic properties of molecular systems including photosynthetic PPCs are often studied via conventional spectroscopic techniques such as steady-state and time-resolved absorption and emission spectroscopy. As the systems of interest become increasingly complex, however, such techniques become of limited use for directly probing electronic energies and couplings and for resolving dynamics in optically congested multichromophoric arrays. In this regard, 2D electronic spectroscopy, based on the heterodyne-detected four-wave mixing technique (49), is one of the most promising recent additions (45, 84–88). In this section, we briefly review the underpinnings of 2D electronic spectroscopic experiments and their applications to the study of light-harvesting systems, especially as they pertain to electronic quantum coherence.

Signals observed in four-wave mixing experiments are related to third-order nonlinear response functions (49) that can be represented as a sum of terms containing three time evolutions of the density matrix to describe electronic excitation. Specifically, 2D electronic spectroscopy based on photon echo measurement involves two types of response functions termed the rephasing and nonrephasing responses. The rephasing response function is expressed approximately as

$$
\begin{aligned}
S_{\mathrm{R}}(t_3,t_2,t_1) \simeq & \sum_{\alpha\beta} \mu_{0\beta} G_{\beta 0}(t_3) \mu_{\beta 0} G_{00\leftarrow 00}(t_2) \mu_{0\alpha} G_{0\alpha}(t_1) \mu_{\alpha 0} \rho_{00} \\
& + \sum_{\alpha\beta\gamma\delta} \mu_{0\delta} G_{\delta 0}(t_3) \mu_{0\gamma} G_{\delta\gamma\leftarrow\beta\alpha}(t_2) \mu_{\beta 0} G_{0\alpha}(t_1) \mu_{\alpha 0} \rho_{00} \\
& - \sum_{\alpha\beta\gamma\delta\bar{\epsilon}} \mu_{\gamma\bar{\epsilon}} G_{\bar{\epsilon}\gamma}(t_3) \mu_{\bar{\epsilon}\delta} G_{\delta\gamma\leftarrow\beta\alpha}(t_2) \mu_{\beta 0} G_{0\alpha}(t_1) \mu_{\alpha 0} \rho_{00},
\end{aligned}
\qquad 15.
$$

where the summations are performed on indices that run over electronic excited states in the one-excitation manifold (e.g., e_α) and in the two-excitation manifold (e.g., $f_{\bar{\epsilon}}$). We note that Equation 15 is an approximate expression of the rephasing response function to provide physical intuition. More rigorous expressions can be found in Reference 49. In the above, $\mu_{\alpha\beta}$ stands for the transition dipole for the $\alpha - \beta$ transition, and $G_{\alpha\beta\leftarrow\gamma\delta}(t)$ is a matrix element of the time-evolution operator given as $\rho_{\alpha\beta}(t) = \sum_{\gamma\delta} G_{\alpha\beta\leftarrow\gamma\delta}(t-s)\rho_{\gamma\delta}(s)$. We have introduced $G_{\alpha\beta}$ as the abbreviation of $G_{\alpha\beta\leftarrow\alpha\beta}$. The nonrephasing response function $S_{\mathrm{NR}}(t_3,t_2,t_1)$ can be obtained by replacing $G_{\delta\gamma\leftarrow\beta\alpha}(t_2)$ and $G_{0\alpha}(t_1)$ by $G_{\delta\gamma\leftarrow\alpha\beta}(t_2)$ and $G_{\alpha 0}(t_1)$, respectively. The graphical method called the double-sided Feynman diagram method is convenient in dealing with complicated expressions for nonlinear optical responses (49). For example, the upper left diagram in **Figure 6** depicts a term in Equation 15, $\mu_{0\beta} G_{\beta 0}(t_3) \mu_{0\alpha} G_{\beta\alpha\leftarrow\beta\alpha}(t_2) \mu_{\beta 0}\, G_{0\alpha}(t_1) \mu_{\alpha 0} \rho_{00}$. This term and its diagram are interpreted as follows: At first the system is in the zero-excitation manifold, $|0\rangle\langle 0|$. The first laser pulse interacts with an exciton state $\langle e_\alpha|$, and then the system is placed into a coherence state, $e^{iE_\alpha t_1/\hbar}\,|0\rangle\langle e_\alpha\,|$, where E_α is the eigenenergy of the αth exciton $|e_\alpha\rangle$. Subsequently, the second pulse interacts with another exciton state $|e_\beta\rangle$, and the system is in a state in the one-excitation manifold during the t_2 period, $e^{-i(E_\beta - E_\alpha)t_2/\hbar}\,|e_\beta\rangle\langle e_\alpha\,|$. The third pulse then interacts again with $\langle e_\alpha|$ to generate a coherence state, $e^{-iE_\beta t_3/\hbar}|\,e_\beta\rangle\,\langle 0\,|$. Other diagrams in **Figure 6** can be interpreted correspondingly. Each diagram has an overall sign of $(-1)^n$, where n is the number of interactions of electric fields with the bra state (49).

2D electronic signals are usually discussed in terms of a 2D frequency map. The most popular choice has been to take the t_1 and t_3 time variables for the Fourier transform, and thus 2D rephasing and nonrephasing spectra are given as $S_{\mathrm{R}}(\omega_3, t_2, \omega_1)$ and $S_{\mathrm{NR}}(\omega_3, t_2, \omega_1)$, respectively. Correspondingly, $G(t_n)$ $(n = 1, 3)$ in the response functions are replaced by $G[\omega_n] \equiv \int_0^\infty dt_n e^{i\omega_n t_n} G(t_n)$. Here, $G_{0\alpha}[\omega_1]$ and $G_{\alpha 0}[\omega_1]$ are linear absorption spectra peaked around $\omega_1 = -E_\alpha/\hbar$ and $E_\alpha/\hbar$, respectively. $G_{\delta 0}[\omega_3]$ corresponds to the spectrum of stimulated emission ($e_\delta \rightarrow 0$) peaked around $\omega_3 = E_\delta/\hbar$, whereas $G_{\bar{\epsilon}\gamma}[\omega_3]$ is that of excited state absorption ($e_\gamma \rightarrow f_{\bar{\epsilon}}$) peaked around $\omega_3 = (E_{\bar{\epsilon}} - E_\gamma)/\hbar$ (**Figure 6**). Notice that $S_{\mathrm{R}}(\omega_3, t_2, -\omega_1)$ and $S_{\mathrm{NR}}(\omega_3, t_2, \omega_1)$ consist of a mixture of absorptive and dispersive components, because they are approximately expressed as products of complex functions, $G[\omega_n]$. Hence, the real part of 2D photon echo spectrum,

$$
S_{\mathrm{PE}}(\omega_3,t_2,\omega_1) \equiv S_{\mathrm{R}}(\omega_3,t_2,-\omega_1) + S_{\mathrm{NR}}(\omega_3,t_2,\omega_1), \qquad 16.
$$

is considered to focus on purely absorptive peaks (89). The only time variable that remains is the so-called waiting time (t_2), and a time-evolution operator of the one-excitation manifold, $G(t_2)$, bridges the absorption spectrum (ω_1) and the stimulated emission/excited absorption spectra (ω_3). Consequently, 2D electronic spectra provide us with visual maps that correlate the electronic energies before and after the waiting interval during which dynamics of electronically excited states takes place. Because the time evolution of the spectrum is spread out onto two dimensions, spectral resolution is

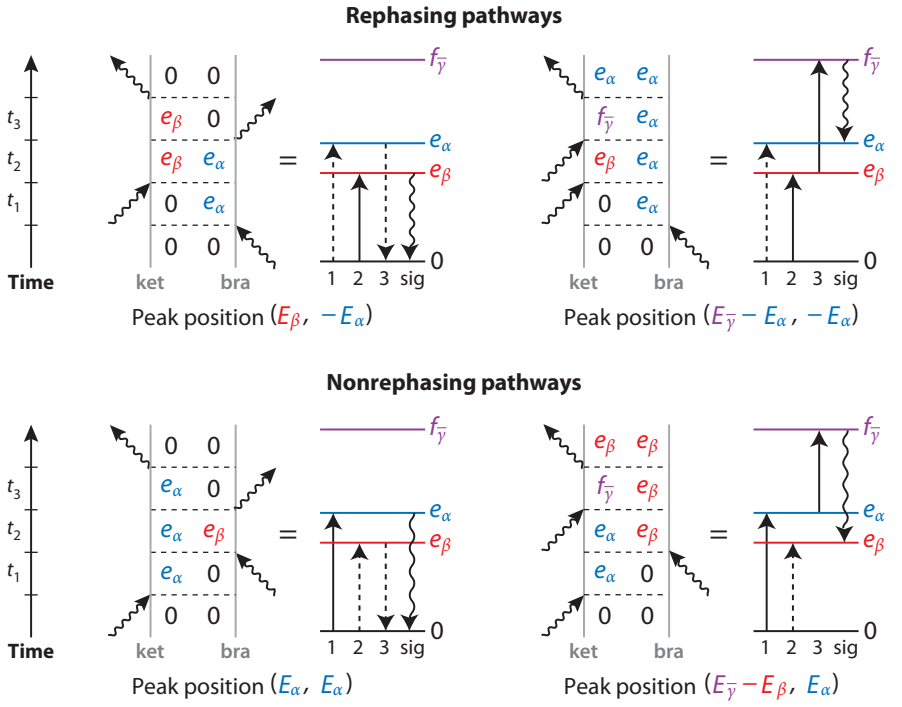

Figure 6

Double-sided Feynman diagrams and their corresponding energy-level diagrams, which represent optical responses giving rise to quantum beats of 2D electronic spectra. In a double-sided Feynman diagram, the time evolution of the density matrix describing electronic excitation is represented by two gray vertical lines labeled ket and bra, where time runs vertically from bottom to top, and wavy arrows represent system-field interactions. 0, e_α, and $f_{\bar{\gamma}}$ represent the overall ground state, an exciton state in the one-excitation manifold, and an exciton state in the two-excitation manifold, respectively. In an energy-level diagram, the solid arrows represent interactions of electric fields with ket states, whereas the dashed arrows represent interactions of electric fields with bra states. In these diagrams, the electronic system is prepared in a coherence state $|e_\beta\rangle\langle e_\alpha|$ or $|e_\alpha\rangle\langle e_\beta|$ during the waiting time, t_2, and hence they contribute to quantum beats in 2D spectra with a frequency $(E_\alpha - E_\beta)/\hbar$. Specifically, the rephasing diagrams (*upper*) contribute to beating of the cross peak $(\omega_1, \omega_3) = (E_\beta, -E_\alpha)/\hbar$, whereas the nonrephasing diagrams (*lower*) give rise to the beats on the diagonal peak $(\omega_1, \omega_3) = (E_\alpha, E_\alpha)/\hbar$.

enhanced and pathways of EET processes are directly revealed as absorption-emission correlation plots (4, 63).

Moreover, broadband laser pulses can interact with all excitons in the one-excitation manifold and create superpositions of the excitons. 2D electronic spectroscopy with the help of the heterodyne-detection scheme records signals at the level of the electric fields generated by samples' polarization rather than the intensity involving their absolute values. The time evolution of a coherence state $|e_\beta\rangle\langle e_\alpha|$ during t_2 has an oscillating phase factor $e^{-i(E_\beta - E_\alpha)t_2/\hbar}$, and hence the presence of electronic coherence manifests itself as quantum beats in 2D spectra (90–92). Consequently, the 2D spectra are sensitive to quantum phase evolution originating from quantum superposition states in the system (5, 7, 8, 41–43, 93, 94). Specifically, diagonal and off-diagonal coherence signals in 2D electronic spectra can be separated through analysis of the rephasing and nonrephasing contributions, respectively. The 2D

rephasing spectrum shows beating of off-diagonal peaks, whereas the 2D nonrephasing spectrum presents beating of diagonal peaks (92, 95). Because the excitons responsible for these beating peaks originate from the electronic excitations on pigments, the coherent dynamics can be mapped back onto the site representation. For a dimer, for example, Equation 10 yields $|e_1\rangle = \cos\theta|1\rangle + \sin\theta|2\rangle$ and $|e_2\rangle = -\sin\theta|1\rangle + \cos\theta|2\rangle$ with θ being the mixing angle defined as $\theta = (1/2)\arctan[2J_{12}/(\Omega_1 - \Omega_2)]$ and $0 \leq |\theta| < \pi/4$. Thus, a time-evolving superposition state, $e^{-iE_1t_2/\hbar}|e_1\rangle + e^{-iE_2t_2/\hbar}|e_2\rangle$, yields a time-dependent probability of finding the state $|1\rangle$ as

$$P_1(t_2) \propto 1 - \sin 2\theta \cdot \cos[(E_1 - E_2)t_2/\hbar]. \quad 17.$$

In this manner, quantum coherence between excitons appears as excitonic wave packet or wave-like energy transfer between the individual pigments, as illustrated in Section 3.3. Here, it should be noted that wave-like motion in the site representation can be obtained only when excitons share the same pigments with a large mixing angle, $|\theta|$. Even if excitons that do not share the same pigments show long-lived superposition, this has absolutely no connection with wave-like energy transfer in the site representation.

4.1. Fenna-Matthews-Olson Complex in Green Sulfur Bacteria

In green sulfur bacteria, the energy transfer between the main chlorosome antenna and the RC complex is mediated by a protein containing bacteriochlorophyll molecules, called the FMO complex (3). The FMO complex is a trimer made of identical subunits, each of which contains bacteriochlorophyll *a* (BChl*a*) molecules (3, 96, 97), as shown in **Figure 7*a***. Until recently, crystallographic studies reported the presence of seven BChl*a* pigments per monomeric subunit. However, recent studies reported the presence of an additional BChl*a* molecule, BChl 8, per subunit (98, 99). BChl 8 is located in a cleft at the surface of the complex, which points toward the chlorosome/baseplate. Therefore, it is considered that this BChl*a* acts as the linker pigment between the FMO complex and the baseplate (100). By virtue of its relatively small size, the FMO complex has represented an important model in photosynthetic EET and has been extensively studied (101–109). Fleming and coworkers (4–6, 110) have investigated EET dynamics in the FMO complex by means of 2D electronic spectroscopy.

Brixner and coworkers (4, 63) investigated EET dynamics in the FMO complex isolated from *Chlorobaculum tepidum*. By analysis of cross-peaks of 2D electronic spectra at multiple waiting times, a visual map of excitation energy flow within the FMO complex was constructed. It reveals two main channels leading to the pooling of excitation energy in the lowest exciton state (63, 108, 111). Furthermore, this experiment demonstrated that excitation energy does not simply cascade stepwise down the excitons' energy ladder. Instead, it depends sensitively on detailed spatial properties of the delocalized excited state wavefunction in terms of the site representation. Naive intuitions about delocalized excitons and their relaxations are not sufficient in understanding photosynthetic EET. Actually, this 2D experiment (4, 63) observed a feature that could not be explained in terms of simple relaxation from an exciton to another. Although References 4 and 63 did not show it explicitly, hints of beating behavior of peaks were seen in the 2D data. Such beating behavior was also observed with use of a fluorescence anisotropy technique (101). These beating behaviors were consolidated by the subsequent theoretical work (91) and systematic experimental investigations (5), and were assigned to an electronic origin, as is described next.

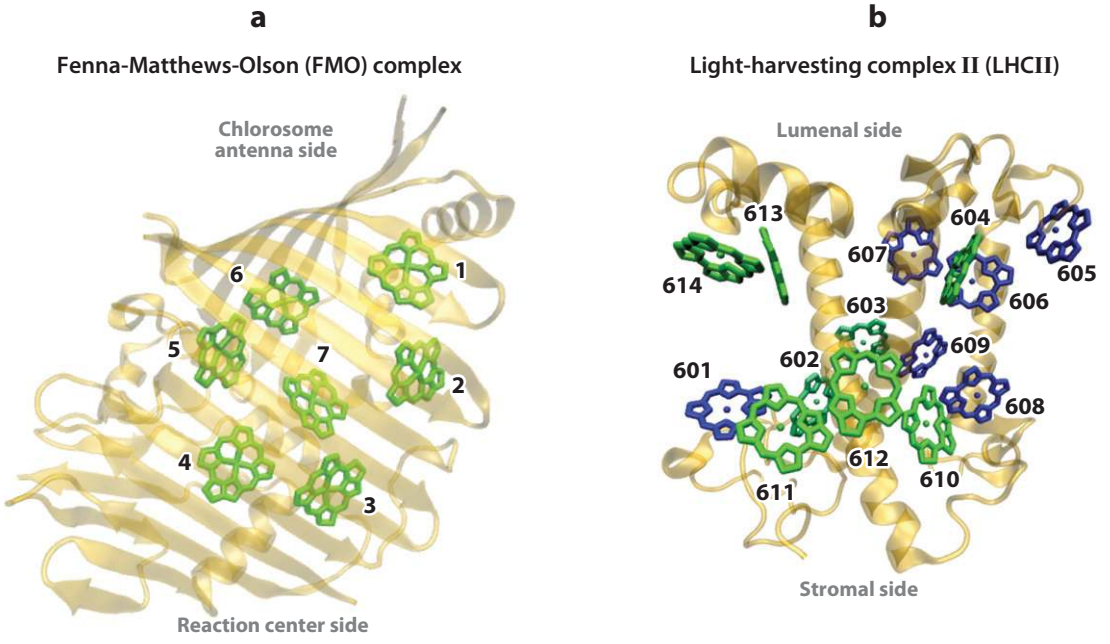

Figure 7

Crystal structures of two of the photosynthetic pigment-protein complexes that have exhibited long-lived electronic quantum coherence: (*a*) a monomeric unit of the FMO complex with BChl*a* in green (PDB ID code 4BCL), and (*b*) a monomeric unit of LHCII with Chl*a* in green and Chl*b* in blue (PDB ID code 1RWT). All proteins are shown in gold. Abbreviations: Bchl*a*, bacteriochlorophyll *a*; Chl*a*, chlorophyll *a*; Chl*b*, chlorophyll *b*; FMO, Fenna-Matthews-Olson; LHCII, light-harvesting complex II; PDB, Protein Data Bank.

Engel et al. (5) explored EET dynamics in the same FMO complex by taking advantage of another ability to be directly sensitive to the quantum phase of a system of interest. This experiment clearly revealed the existence of long-lived quantum coherence among the electronic excited states of the multiple pigments in the FMO complex at 77 K. The observed coherence clearly lasts for at least 660 fs, although it is generally believed that electronic coherence decays on the 10–100 fs timescales (85, 112). The timescale of the observed coherence is similar to the EET timescales, implying that electronic excitations travel coherently though the FMO complex rather than by incoherent diffusive motion, as has usually been assumed (72). This experimental result spawned a burst of investigations of quantum mechanical effects in biological systems, in particular in photosynthetic light harvesting.

4.2. Reaction Center Complex in Purple Bacteria

Much of the recent work regarding electronic quantum coherence in photosynthetic systems takes the FMO complex as a prototype system. However, observation of long-lasting quantum coherence is not unique to the FMO complex. Lee et al. (10) revealed long-lived quantum coherence between bacteriochlorophyll and bacteriopheophytin in the RC of purple bacterium, *Rhodobacter sphaeroides*, by applying a two-color electronic coherent photon echo technique. This measurement yielded dephasing times of 440 and 310 fs at temperatures of 77 and 180 K, respectively. Most notably, it was clearly demonstrated that strongly

correlated fluctuations in the pigments' site energies can enable long-lasting coherence, although traditional theoretical models of photosynthetic EET assume that each site of a multichromophoric array is coupled to its local environmental DOFs. If fluctuations in electronic states of different pigments are correlated or almost synchronized, the EET process among the pigments would not experience any noise or dynamic disturbance. In this situation, the phase coherence of the quantum mechanical wave packet involved in the EET process would be preserved. It is interesting that this preservation of electronic quantum coherence is similar to the notion of noiseless quantum codes (113) or decoherence-free subspace (DFS) (114, 115) developed in the community of quantum information science. Theories of the DFS have provided an important strategy for the passive preservation of quantum information. Specifically, the correlated fluctuation effect for preserving quantum coherence corresponds to the weak collective DFS proposed by Kempe et al. (116). This discovery stimulated much of the subsequent theoretical work regarding the correlated fluctuation effects upon EET dynamics (12, 19, 20, 23, 31, 34, 35, 117).

Figure 8 illustrates how the dimer system discussed in **Figure 5** varies for different extremes of environmental correlation (23, 44). Similar to **Figure 5**, the adiabatic exciton potential surfaces are drawn as a function of two phonon coordinates with minima representing two electronic states. In the case of positive correlation (**Figure 8*a***) the minima move into the same quadrant reducing their spacing and hence the energy barrier between them. A Franck-Condon transition to the origin lies above the energy barrier resulting in a delocalized excited state promoting coherence, and hence the EET is robust against environment-induced fluctuations (23). However, for the negative correlation case illustrated in **Figure 8*b***, the minima exist in opposite quadrants. The large energy barrier between them results in a localized

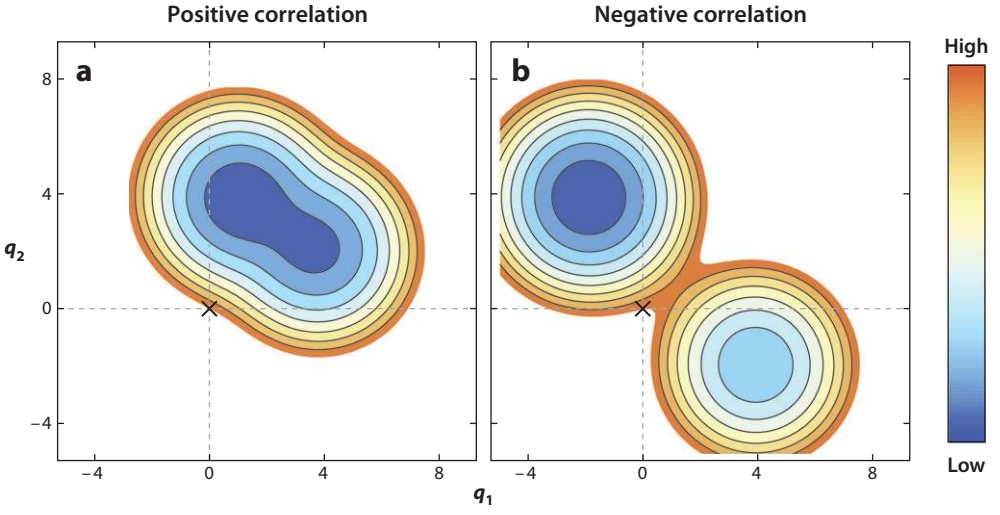

Figure 8

Adiabatic excitonic potential surfaces for the cases of (*a*) positive and (*b*) negative correlated fluctuations. We consider the following instead of Equations 13: $\epsilon_m(\mathbf{q}) = \epsilon_0(\mathbf{q}) + \hbar\Omega_m - \hbar\omega_{\rm ph} dq_m - \hbar\omega_{\rm ph}\zeta_m dq_n$ for $m \neq n$, where the collective energy gap coordinates can be expressed as $u_m = -\hbar\omega_{\rm ph} dq_m - \hbar\omega_{\rm ph}\zeta_m dq_n$. As a result, the auto-correlation function of $u_m(t)$ is obtained as $\langle u_m(t)u_m(0)\rangle = (1+\zeta_m^2)C_{qq}(t)$, whereas the cross-correlation function is $\langle u_m(t)u_n(0)\rangle = (\zeta_m + \zeta_n)C_{qq}(t)$. Here, $C_{qq}(t) \equiv \hbar^2\omega_{\rm ph} d^2\langle q_m(t)q_m(0)\rangle$ has been introduced independently of the values of m for simplicity. We have chosen $\zeta_1 = \zeta_2 = 0.5$ for panel *a* and $\zeta_1 = \zeta_2 = -0.5$ for panel *b*. The other parameters are the same as in **Figure 5.**

state upon excitation to the origin thus eliminating coherence, and hence the EET becomes slower or more inefficient because the EET must overcome a higher energy barrier between the two states (23).

4.3. Light-Harvesting Complex II in Green Plants

The significance of quantum coherence to photosynthetic EET cannot be argued without it first being established as a universal phenomenon. If coherence is essential for photosynthetic light harvesting, it should be present in the large antenna complexes whose sole responsibility is to absorb solar energy and funnel it to the RCs. Despite having energy transfer as its primary function, the FMO complex and the bacterial RC are not key photosynthetic complexes. This raises the question as to whether electronic quantum coherent motion of excitation energy was a universal phenomenon in photosynthesis.

Calhoun et al. (43) addressed this issue, applying 2D electronic spectroscopic measurement to LHCII of *Arabidopsis thaliana*. LHCII is the major light-harvesting complex of green plants and contains more than 50% of all chlorophyll molecules on Earth, making it well suited to answer the above question. The structure of LHCII is trimeric with each monomer containing eight chlorophyll *a* (Chl*a*) molecules and six chlorophyll *b* (Chl*b*) molecules (118–123), as shown in **Figure 7*b***. Calhoun et al. explored the 2D nonrephasing spectra by taking advantage of the fact that diagonal peaks in the 2D spectra originate from the nonrephasing pathways (92). Evolution of the diagonal cuts of the 2D nonrephasing spectra as a function of the waiting time (t_2) provides a means to specifically probe the coherent phase evolution prepared by the first two laser pulses in the four-wave measurement. **Figure 9*a*** gives the real part of the 2D nonrephasing spectrum for $t_2 = 250$ fs at 77 K, and **Figure 9*b*** presents the diagonal cuts of the 2D nonrephasing spectra as a function of the waiting time, t_2. Quantum beats due to excitonic coherence are clearly visible for the 500 fs duration of the experiment in the more intense Chl*a* region on the left and in the weaker Chl*b* signal on the right. Furthermore, Calhoun et al. demonstrated that Fourier transform along the t_2-axis produced a coherence power spectrum by which the excitonic

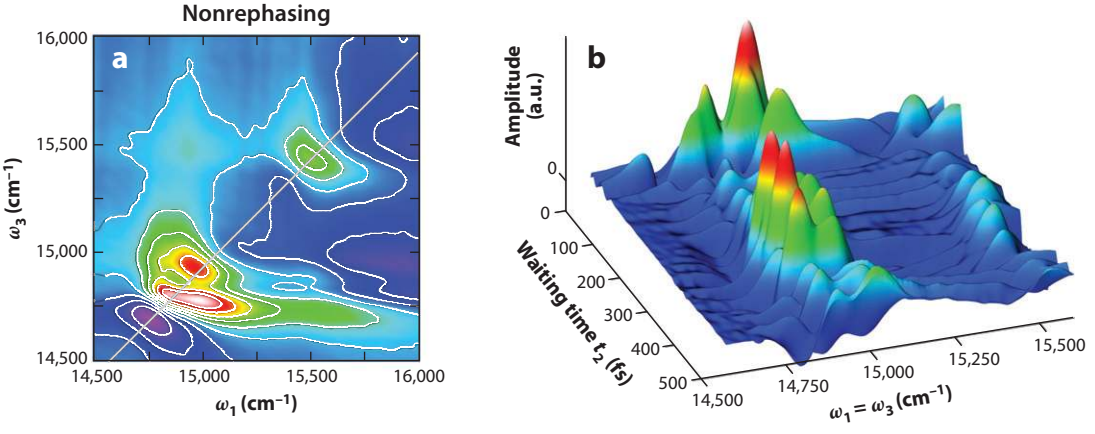

Figure 9

(*a*) The real part of the 2D nonrephasing spectrum of light-harvesting complex II (LHCII) at the waiting time $t_2 = 250$ fs. (*b*) The amplitude of the diagonal cut (*gray line* in panel *a*) of the 2D nonrephasing spectra as a function of waiting time. For panels *a* and *b*, the amplitude increases from purple (negative) to white (positive). Figure taken from Reference 43.

energy levels in LHCII could be experimentally visualized and hence extracted for the first time despite the congested spectra (43).

4.4. Quantum Coherence at Ambient Temperatures: Marine Algae and the Fenna-Matthews-Olson Complex

Discoveries of long-lasting electronic quantum coherence in the FMO complex (5), the bacterial RC (10), and LHCII of green plant (43) provide valuable insights into the inner workings of photosynthetic light-harvesting systems. However, the measurements were performed outside the physiological range of temperatures. Generally, it is believed that quantum coherence at physiological temperatures is fragile compared to that at cryogenic temperatures because amplitudes of environmental fluctuations increase with increasing temperature. For instance, the root-mean-square amplitude of the electronic energy gap fluctuation (Equation 4) can be estimated via the FDR (Equation 5) as $\hbar\Delta_m \equiv \sqrt{\langle u_m^2 \rangle_{mg}} \simeq \sqrt{2\hbar\lambda_m/\beta}$. Hence, the robustness of electronic quantum coherence under physiological conditions is still a matter of ongoing investigation.

Collini et al. (41) investigated marine algae called cryptophytes. 2D electronic spectroscopic measurements were conducted for two evolutionally related light-harvesting antenna complexes, phycoerythrin 545 from *Rhodomonas* CS24 and phycocyanin 645 from *Chroomonas* CCMP270, at ambient temperature 294 K. Both phycoerythrin 545 and phycocyanin 645 contain eight light-absorbing bilin molecules covalently bound to the protein scaffold. The observation provided compelling evidence for the involvement of quantum coherence in light harvesting at physiologically relevant conditions.

Furthermore, Panitchayangkoon et al. (42) extended the previous 2D experiment of the FMO complex (5) up to 277 K and examined in detail the temperature dependence of the quantum coherence lifetimes. **Figure 10** presents the real parts of 2D electronic photon echo spectra of the FMO complex at the waiting time $t_2 = 400$ fs and 77 K (*a*), 125 K (*b*), 150 K (*c*), and 277 K (*d*). **Figure 10*e*** shows the absolute value of the amplitude of the highlighted cross-peak, which indicates the location of $e_1 - e_3$ cross-peak, as a function of waiting time for each temperature. From these results, one clearly observes that electronic quantum coherence lasts up to 300 fs even at physiological temperatures 277 K. This lifetime is consistent with theoretical prediction for the same FMO complex (17), as shown in **Figure 11.** The numerical calculations were performed on the basis of the excitation-environment coupling parameters adopted for simultaneous fitting of linear and 2D rephasing, nonrephasing, and polarization-dependent electronic spectra (110), i.e., $\lambda_m = 35\ \mathrm{cm}^{-1}$ and $\tau_m^{\mathrm{rxn}} = 50\,\mathrm{fs}(1/\tau_m^{\mathrm{rxn}} = 106\,\mathrm{cm}^{-1})$ are the values of reorganization energy and relaxation time. The excitation Hamiltonian was taken from Reference 108.

5. HOW DOES QUANTUM MECHANICS WORK IN PHOTOSYNTHETIC LIGHT HARVESTING?

5.1. Quantum Coherence in Photosynthetic Systems

The growing body of evidence for electronic quantum coherence in photosynthetic EET has invigorated discussion concerning electronic quantum coherence within photosynthetic PPCs and its relation to light-harvesting efficiency. One of the roles conjectured for electronic quantum coherence in photosynthetic systems was a speed-up in the search for the lowest

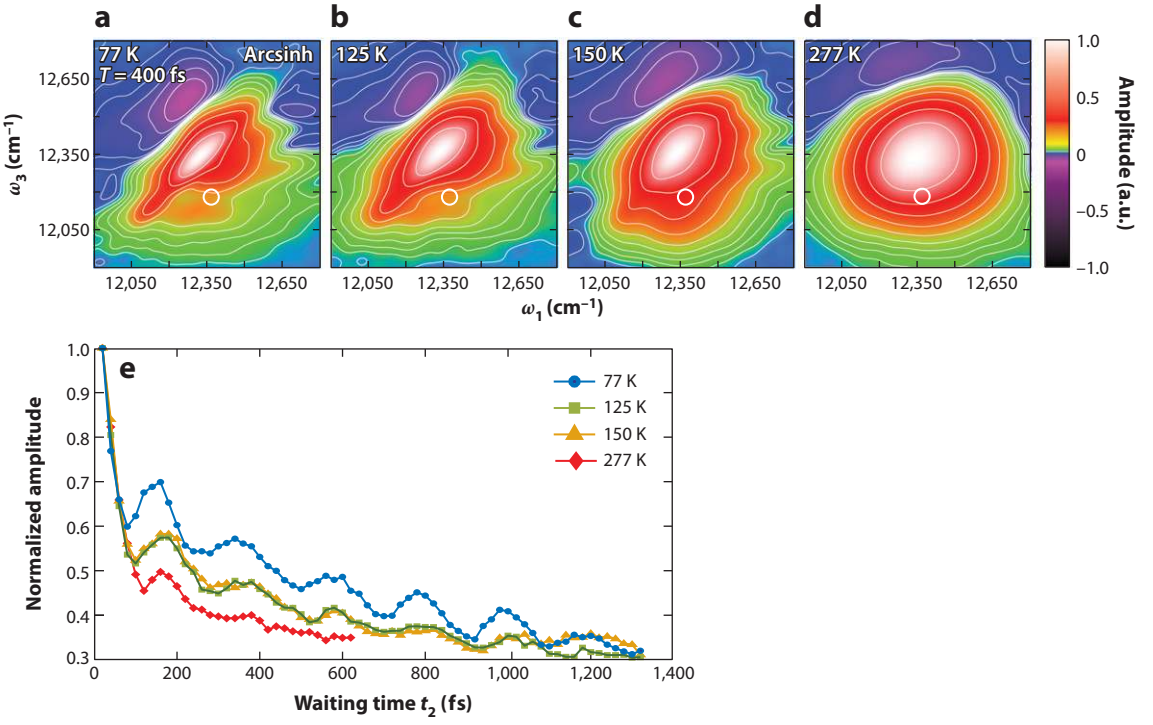

Figure 10

The real parts of 2D electronic photon echo spectra of the Fenna-Matthews-Olson (FMO) complex of *Chlorobaculum tepidum* are shown at the waiting times $t_2 = 400$ fs and 77 K (*a*), 125 K (*b*), 150 K (*c*), and 277 K (*d*). The data are shown with an arcsinh color scale to highlight small features in both negative and positive portions. Peaks broaden at higher temperatures due to faster dephasing. The quantum beat signals are extracted at the spectral position (*white circle*) corresponding to the location of $e_1 - e_3$ cross-peak. The beating signals (*e*) demonstrate agreement in phase and beating frequency among all four temperatures and show shorter quantum beat lifetimes at higher temperatures. Figure taken from Reference 42.

energy state in a process analogous to Grover's quantum search algorithm (124), which is known to exhibit a quadratic speed-up over its classical counterparts for searching elements in a database (5, 125). This fascinating speculation inspired several works (7–40). Mohseni et al. (11) argued that a purely unitary Grover-type search algorithm is not able to explain the EET efficiency in the FMO complex. A Hamiltonian generating Grover's algorithm should map an equal coherent superposition of all possible database states onto a desired target state, within a time polynomial in the size of the database and with a probability close to 1. Nevertheless, the coherent Hamiltonian dynamics does not result in a significant overlap to BChls 3 and 4 facing the RC complex, when an electronic excitation is input on BChls 1 or 6 close to the chlorosome antenna (108, 111), where we have used the usual numbering of the BChls (3). However, Mohseni et al. suggested that certain non-unitary generalizations of quantum search algorithms could be developed to be relevant in this context.

By mapping the EET dynamics onto one-dimensional quantum walks, Hoyer et al. (33) examined the limits of the quantum speed-up mechanism of the FMO complex in the sense of quantum search algorithms. This work demonstrated that the EET dynamics exhibits ballistic transport and correspondingly a quadratic quantum speed-up only at short times, ∼70 fs, although the electronic quantum coherence survives for hundreds of femtoseconds (5, 17, 42).

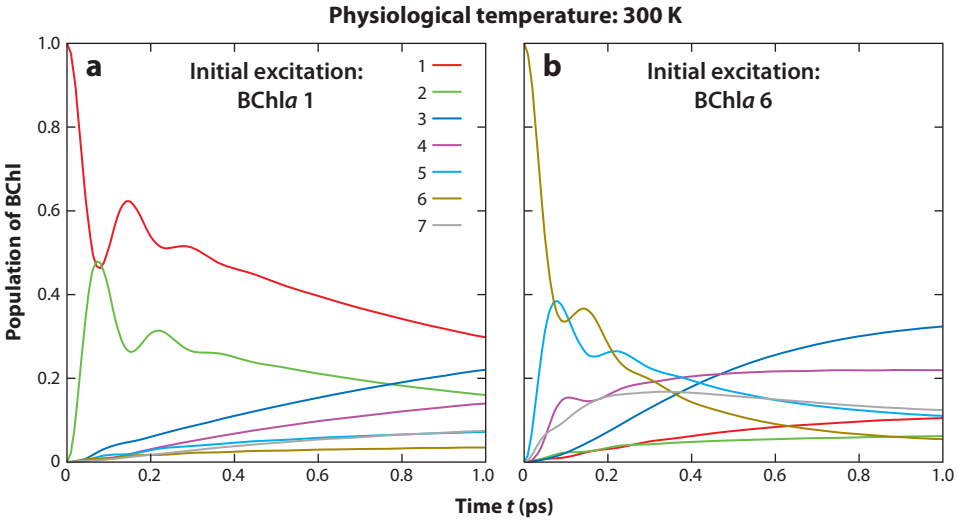

Figure 11

Time evolution of the electronic excitation on each BChl*a* in the FMO complex of *Chlorobaculum tepidum*. Calculations were performed for physiological temperature 300 K, on the basis of the one-excitation Hamiltonian given in Reference 108. The reorganization energy and the environmental relaxation times are set to be $\lambda_m = 35\ \mathrm{cm}^{-1}$ and $\tau_m^{\mathrm{rxn}} = 50\ \mathrm{fs}$, which were obtained from analyses of 2D electronic spectra of the FMO complex (110). BChl*a* 1 (*a*) and BChl*a* 6 (*b*) are adopted as the initial excited pigment for numerical calculations. Figure taken from Reference 17. Abbreviations: BChl*a*, bacteriochlorophyll *a*; FMO, Fenna-Matthews-Olson.

On the basis of this observation, it was concluded that the quantum coherence in the FMO complex was more likely to contribute to other aspects of transport, such as overall efficiency or robustness, instead of yielding quantum speed-up in the sense of quantum information processing.

Indeed, Ishizaki & Fleming (17) discussed the robustness of the efficient EET dynamics. They argued that the FMO complex aids efficient energy flow from the chlorosome antenna to the RC by taking advantage of interplay among quantum coherence, environment-induced fluctuations and dissipation, and energy landscape of pigments' site energies tuned by the protein scaffold. The basic idea is as follows: If the EET were dominated only by diffusive incoherent hopping, trapping in subsidiary energetic minima would be inevitable. However, quantum delocalization can allow avoidance of the traps to aid the subsequent trapping of excitation by the pigments facing the RC. Incoherent hopping processes involve a thermal activation process to overcome an energy barrier separating pigments, as demonstrated in **Figures 5** and **8.** This hopping process is described as a stochastic process controlled by environment-induced fluctuations and temperatures. However, coherent energy transfer or quantum delocalization does not experience such an energy barrier, as discussed in Section 3.3. Of course, quantum mechanics is a probabilistic theory in the sense that it provides a scheme for predicting the probabilistic distribution of the outcome of measurements made on suitably prepared copies of a system. However, this randomness inherent in quantum mechanics is different from the stochasticity caused by the environment-induced fluctuations. In the sense that electronic couplings among pigments act as driving forces or waveguides of EET dynamics, quantum coherent EET can be regarded as deterministic in comparison with the diffusive

incoherent hopping EET. On the basis of this viewpoint, Ishizaki & Fleming suggested that quantum coherence allows the FMO complex to work as a rectifier or ratchet for unidirectional energy flow from the chlorosome antenna to the RC as follows: In general, unidirectional energy flow facilitates the achievement of a near-unity quantum yield. For the unidirectionality, once excitation migrates to the linker pigments between a light-harvesting PPC and an RC, it has to be trapped and directed to the RC (110). Therefore, it is usually thought that photosynthetic PPCs rapidly funnel down electronic excitation energy toward the RC. Indeed, LHCII in higher plants creates a steep electronic energy landscape with use of two variants of pigment, Chl*a* and Chl*b* (120, 123). However, the FMO complex of green sulfur bacteria comprises only one type of pigment, BChl*a*, and therefore the energy landscape therein is relatively flat compared to k_BT at physiological temperatures, where k_B and T are the Boltzmann constant and temperature. Such a flat energy landscape would allow facile backward transfer of excitation away from the RC at physiological temperatures. This consideration led Ishizaki & Fleming (17) to speculate that an uphill energetic step along EET pathways in the FMO complex (**Figure 12**) might be designed to make the steepest possible energy landscape and to avoid the backward transfer. The electronic couplings work as driving forces for the EET regardless of whether EET is uphill or downhill, and hence the detrapping of excitation on the subsidiary energetic minimum (BChl 1) is avoided with the help of quantum coherence, as shown in **Figure 11*a***.

The arguments concerning quantum coherence in the FMO complex by Aspuru-Guzik and coworkers (11, 12, 27) and Plenio and coworkers (28, 35) are also related to the robustness of EET dynamics induced by the interplay between quantum coherence and environment-induced noise leading to efficient EET. By employing a pure dephasing model such as the Haken-Strobl model (126), Rebentrost et al. (27) vividly illustrated this interplay. In a

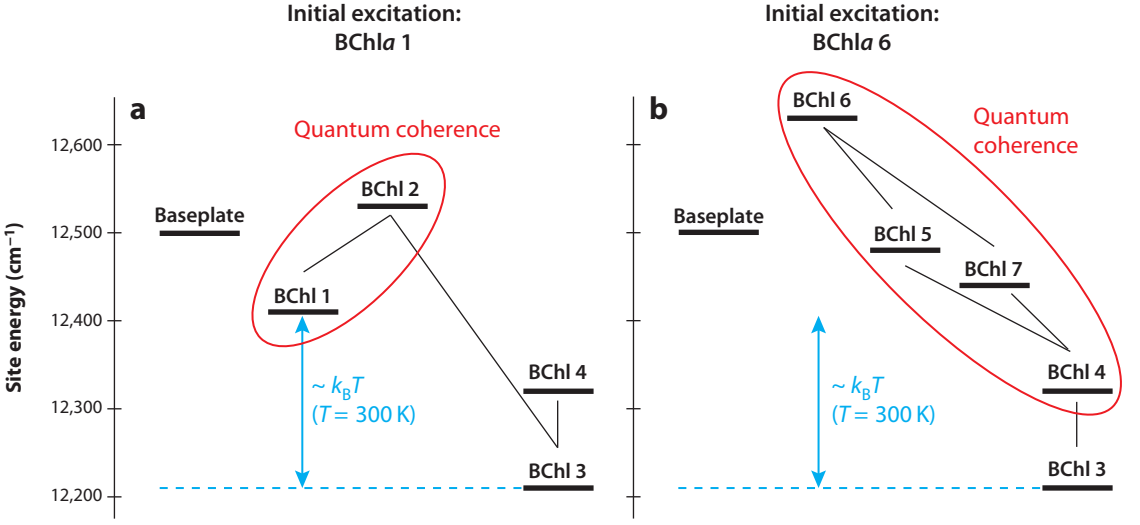

Figure 12

The energy landscapes along the two primary transfer pathways in the FMO complex: (*a*) baseplate → BChl*a* 1 → 2 → 3 → 4 and (*b*) baseplate → BChl*a* 6 → 5, 7, 4 → 3. We employ the one-excitation Hamiltonian for the trimeric structure of the FMO complex published in Reference 108. The relatively strong electronic couplings between BChl*a* molecules are depicted by solid lines, and pigments that make quantum superpositions are circled in red. Figure taken from Reference 17. Abbreviations: Bchl*a*, bacteriochlorophyll *a*; FMO, Fenna-Matthews-Olson.

quantum system with some degree of disorder such as the FMO complex, destructive interference caused by the Anderson localization suppresses quantum transport efficiency at low noise levels. At very high noise levels, however, decoherence effectively produces the quantum Zeno effect (127) that also suppresses transport phenomena. At intermediate noise levels, however, coherence and decoherence can collaborate to produce highly efficient transport. The authors demonstrated that the FMO complex at physiological temperatures is in this intermediate noise state.

5.2. Quantum Entanglement in Photosynthetic Systems

The experimental evidence and theoretical examinations for long-lived electronic quantum coherence have motivated several groups to explore quantum entanglement, which is a particularly peculiar form of quantum correlation, in photosynthetic light-harvesting systems (21–24, 35–38). To explore quantum entanglement among electronic excitations of the BChl*a* molecules in the FMO complex, Sarovar et al. (22) derived a measure of global entanglement for the one-excitation manifold with the help of the relative entropy of entanglement (128). It was shown that excitation that is initially localized on one of the pigments evolves toward entangled states and these entangled states have long lifetimes on the picosecond timescale even at physiological temperatures. The lifetimes of the entangled states are limited only by the trapping by the RC, which is assumed to have a rate of $(4\ \mathrm{ps})^{-1}$ in the calculations.[1] Furthermore, detailed analyses of bipartite entanglement were performed by means of the concurrence (129). Notably, the concurrence measure revealed that nonvanishing entanglement is generated and maintained between BChls 1 and 3 separated by $\sim$30 Å, which is the second largest separation distance in the FMO complex. In summary, Reference 22 showed that the quantum entanglement in the one-excitation manifold is robust, contrary to expectation.

To clarify the reason for nonvanishing entanglement in photosynthetic PPCs, we focus on the simplest entanglement measure, the concurrence (129) for a dimer composed of pigments 1 and 2. Within the one-excitation manifold, the concurrence reduces to the simple form (22, 23)

$$\mathcal{C} = 2\,|\langle 1\,|\,\rho\,|\,2\rangle|, \qquad 18.$$

with ρ being the density operator describing electronic excitation. Expressions of the other entanglement measures in the one-excitation manifold, e.g., the logarithmic negativity (35, 36), are also comprised of off-diagonal elements of the density matrix in the site representation. Note that $|m\rangle = |\varphi_{me}\rangle\prod_{k(\neq m)}|\varphi_{kg}\rangle$ is not an eigenstate of the excitation Hamiltonian because of the presence of the electronic coupling J_{mn}. Therefore, off-diagonal elements of the density matrices in the site representation do not necessarily vanish, and thus it is not surprising that Equation 18 shows finite values in the steady state, i.e., the presence of robust entanglement. Actually, spectroscopically detectable delocalized excitons (Equations 10 and 11) are entangled states as long as one follows the mathematical definition of quantum entanglement (130). The effect of finite temperatures upon the nonvanishing entanglement is explained by the following simple argument. For a dimer, Equation 10 yields $|e_1\rangle = \cos\theta|1\rangle + \sin\theta|2\rangle$ and $|e_2\rangle = -\sin\theta|1\rangle + \cos\theta|2\rangle$, with θ being the mixing angle defined as $\theta = (1/2)\arctan[2J_{12}/(\Omega_1 - \Omega_2)]$ and $0 \leq |\theta| < \pi/4$. The steady state in this system is assumed to be nearly in the

[1]To avoid misconception, we note that we do not have experimental evidence regarding the rate constant of trapping by the RC in this system.

canonical distribution in the exciton representation, and therefore one gets a temperature-dependent expression for $\langle 1 | \rho | 2 \rangle$ of

$$\langle 1 | \rho | 2 \rangle = -J_{12} \frac{\tanh\left[(\beta\hbar/2)\sqrt{(\Omega_1 - \Omega_2)^2 + 4J_{12}^2}\right]}{\sqrt{(\Omega_1 - \Omega_2)^2 + 4J_{12}^2}}. \quad 19.$$

This simple expression captures the following important features regarding the concurrence in the one-excitation manifold:

$$\lim_{\beta\to 0} \mathcal{C} = 0, \quad \lim_{\beta\to\infty} \mathcal{C} = 1, \quad \lim_{\theta\to 0} \mathcal{C} = 0, \text{ and } \quad \lim_{|\theta|\to\pi/4} \mathcal{C} = 1, \quad 20.$$

as demonstrated by means of more accurate numerical calculations (23). That is to say, one can have nonvanishing entanglement in the single excitation manifold in the case of nonzero electronic coupling and finite temperature. However, temperature-independent pure dephasing models include no dissipation effect, i.e., $\Gamma_m(t) = 0$. The FDR in Equation 5 indicates that this situation corresponds to infinite temperature, $\beta \to 0$, making statements of long-lived entanglement based on these approaches inappropriate.

As is clear from this discussion, quantum entanglement in photosynthetic PPCs and spectroscopically detectable delocalized excitons are inextricably related, and hence nonvanishing entanglement is expected. Therefore, it is difficult to separate the two phenomena and to ascribe a functional role to one versus the other. Having said that, Reference 23 demonstrated that investigations with tools quantifying the entanglement may provide us with more detailed information on the nature of quantum delocalized states, in particular on dynamic localization (131), and correlated fluctuation effects, which are difficult for a traditional treatment such as the inverse participation ratio (132) to capture. In general an exciton in the two-excitation manifold (Equation 11) cannot be expressed as a product state of excitons in the one-excitation manifold such as $|f_{\bar{\alpha}}\rangle \propto |e_\beta\rangle |e_\gamma\rangle$. In regard to this point, Mukamel (25) explored quantum entanglement in nonlinear optical responses. Other tests and measures of the quantum correlation in photosynthetic PPCs were also examined, e.g., violations of the Leggett-Garg inequality (39, 133) and the dynamics of quantum discord (40, 134).

6. TOWARD ATOMIC-LEVEL DESCRIPTIONS OF PHOTOSYNTHETIC ENERGY TRANSFER DYNAMICS

One of the viable approaches to explore photosynthetic EET is the reduced density matrix (RDM), i.e., the partial average of the total density matrix over the environmental DOFs. Approaches of this type have a considerable domain of applicability and have provided useful insights into condensed phase spectra and photosynthetic EET (49, 72). However, the RDM approach has a model character and is most often not directly connected to an atomic-level description of the system of interest, and therefore the approach might fail to capture chemically/biologically important aspects. The great strides in computer power have enabled us to perform full-atom quantum dynamics calculations for small systems. For systems with a large number of DOFs, however, it is still extremely difficult to apply such calculations. Thus, it is common that only the important DOFs are treated quantum mechanically, whereas the others are treated classically (135). Unfortunately, however, the boundary

between quantum and classical descriptions, which is set in an ad hoc fashion, may cause severe problems because the inherent effects of quantum interference cannot be treated appropriately.

Recently, the validity of such a mixed quantum/classical approach for describing EET was examined (136). In the approach, only the electronic excitation is treated quantum mechanically, whereas the environmental DOFs are described as classical variables. Classical noise in this model forces the electronic excitation to remain in a pure quantum state. This approach corresponds to a pure dephasing model such as the Haken-Strobl model (27, 29, 30, 33, 59, 126, 137). **Figure 13** shows the ensemble average of excitation dynamics influenced by classical noise in the FMO protein. We employed the same one-excitation Hamiltonian (108) and the same excitation-environment coupling parameters used for the RDM results presented in **Figure 11**. Both panels in **Figure 13** demonstrate that the ensemble average and the RDM show excellent agreement with respect to quantum coherent wave-like behavior and its destruction. However, a clear difference is observed in the longer time region. This difference is explained by the breakdown of the FDR in the pure-dephasing model (136), as discussed in Section 5.2. Despite this reasonable artifact, the agreement in terms of the quantum coherent motion hints at the possibility of an atomic-level description of electronic quantum coherence and its interplay with protein environments in photosynthetic electronic energy transfer. Recently, Kelly & Rhee (138) obtained a similar result by employing the quantum-classical Liouville equation approach (139). Tao & Miller (76), on the basis of the linearized

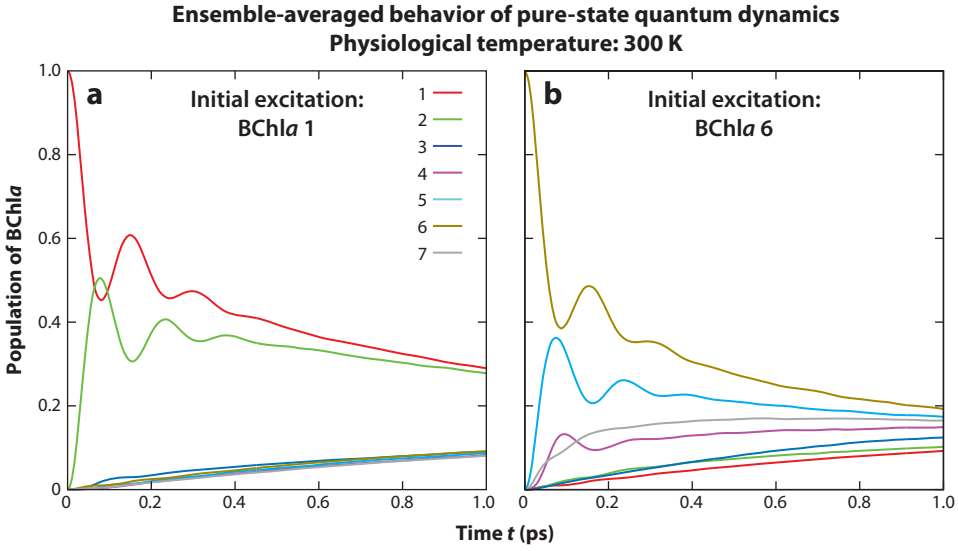

Figure 13

Ensemble-averaged time evolution of a population of each BChl*a* molecule in the FMO complex of *Chlorobaculum tepidum*. Calculations were performed for physiological temperature 300 K. The mixed quantum/classical approaches corresponding to a pure dephasing model were employed, and hence no decoherence process is involved. BChl*a* 1 (*a*) and BChl*a* 6 (*b*) are adopted as the initial excited pigment for numerical calculations. The one-excitation Hamiltonian and excitation-environment coupling parameters used in these calculations are the same as those in **Figure 11**. We followed the discretization procedure of the spectral density described by Reference 150 with 1,000 phonon modes per site. Abbreviations: Bchl*a*, bacteriochlorophyll *a*; FMO, Fenna-Matthews-Olson.

semiclassical initial value representation approach, also made an important step toward the all-atom simulation.

7. CONCLUDING REMARKS

A growing body of evidence for electronic quantum coherence in photosynthetic light-harvesting systems has invigorated discussions concerning quantum mechanical effects during photosynthetic EET and its relation with light-harvesting efficiency. Yet, it is not clear whether quantum mechanical effects generally play significant and nontrivial roles in biological organisms.

In a monograph entitled *What is Life?* (140), Erwin Schrödinger stated as follows: "As we shall presently see, incredibly small groups of atoms, much too small to display exact statistical laws, do play a dominating role in the very orderly and lawful events within a living organism." This statement suggests that quantum mechanisms may underlie the remarkably high quantum efficiency of photosynthetic EET. Experimentally, photosynthetic EET dynamics is investigated by synchronizing initial electronic excitation in the entire ensemble by means of ultrashort laser pulses. In natural light harvesting, however, the initial event is the absorption of one sunlight photon by a single PPC, followed by EET in the PPC independently of the ensemble-averaged behavior or our measurements. Hence, it will be intriguing to explore the dynamics of electronic excitation wave packets in a single photosynthetic PPC or a dilute ensemble far from the thermodynamic limit. It is becoming possible to merge ultrafast spectroscopy and single-molecule detection (141–144). Recently, van Hulst and coworkers (143, 144) reported the observation of vibrational wave packets in individual molecules at ambient temperatures by means of the phase-locked spontaneous light emission technique (145–148). Applications of this technique to the detection of electronic quantum coherence or electronic wave packet interferometry in individual PPCs will provide further insights into photosynthetic EET. Furthermore they should enrich our understanding of fundamental aspects of quantum mechanics such as decoherence.

Further Schrödinger said, "A single group of atoms existing only in one copy produces orderly events, marvelously tuned in with each other and with the environment according to most subtle laws" (140). The subtlety hinted at in this comment is exemplified by the role of the protein in photosynthesis, in particular by modification of cofactor properties, preservation of coherence, and tuning of electron-phonon coupling to produce emergent properties of the system. A striking example occurs in the electron transfer chains of plant and cyanobacterial photosystems I and II (PSI and PSII). The same molecule, chlorophyll *a*, is used as the strongest reducing agent in nature in PSI and the strongest oxidizing agent in nature in PSII. The model nature of the RDM approach limits the extent to which local environmental effects such as those noted by Groot et al. (149) can be investigated. One needs to explore individual proteins embedding pigments not only as randomly fluctuating dissipative environments from the statistical physical point of view as is usual in the literature of photosynthetic EET, but also as functional environments on the basis of atomic-level understanding with the help of comprehensive investigations combining quantum dynamic theories with quantum chemical calculations and molecular dynamics simulations. Recent studies by Olbrich et al. (31, 32) are along these lines. This standpoint should enable a deepening of our understanding not only of the remarkably high efficiency of photosynthetic light harvesting, but also of stochasticity and selectivity in the molecular world, in particular directionality or autonomy dominating biophysical/biochemical events.

Lastly, we note that the role of the photosynthetic apparatus is not limited to efficiently transporting excitation energy toward RC complexes, although many studies of quantum coherence in photosynthetic EET have paid attention only to this aspect. At high light intensities, however, many light-harvesting systems have regulation mechanisms that initiate quenching of excess excitation energy to mitigate oxidative damage and protect RCs. Because highly reactive chemical species are inevitable by-products of photosynthesis, such regulatory processes are critical for the robustness of photosynthesis. It will be intriguing to address such photoprotection mechanisms from the combined multidisciplinary viewpoints of quantum physics and condensed phase chemistry.

DISCLOSURE STATEMENT

The authors are not aware of any affiliations, memberships, funding, or financial holdings that might be perceived as affecting the objectivity of this review.

ACKNOWLEDGMENTS

This work was supported by the Director, Office of Science, and Office of Basic Energy Sciences of the U.S. Department of Energy under contract DE-AC02-05CH11231 and by the Division of Chemical Sciences, Geosciences, and Biosciences and Office of Basic Energy Sciences of the U.S. Department of Energy through grant DE-AC03-76SF000098. A.I. is grateful for financial support of the Postdoctoral Fellowship for Research Abroad by the Japan Society for the Promotion of Science (2008–2010).

LITERATURE CITED

1. Blankenship RE. 2002. *Molecular Mechanisms of Photosynthesis*. London: World Sci.
2. Horton P, Ruban AV, Walters RG. 1996. *Annu. Rev. Plant Physiol. Plant Mol. Biol.* 47:655–84
3. Fenna RE, Matthews BW. 1975. *Nature* 258:573–77
4. Brixner T, Stenger J, Vaswani HM, Cho M, Blankenship RE, Fleming GR. 2005. *Nature* 434:625–28
5. Engel GS, Calhoun TR, Read EL, Ahn TK, Mančal T, et al. 2007. *Nature* 446:782–86
6. Read EL, Engel GS, Calhoun TR, Mančal T, Ahn TK, et al. 2007. *Proc. Natl. Acad. Sci. USA* 104:14203–8
7. Womick JM, Moran AM. 2009. *J. Phys. Chem. B* 113:15747–59
8. Womick JM, Moran AM. 2009. *J. Phys. Chem. B* 113:15771–82
9. Myers JA, Lewis KLM, Fuller FD, Tekavec PF, Yocum CF, Ogilvie JP. 2010. *J. Phys. Chem. Lett.* 1:2774–80
10. Lee H, Cheng YC, Fleming GR. 2007. *Science* 316:1462–65
11. Mohseni M, Rebentrost P, Lloyd S, Aspuru-Guzik A. 2008. *J. Chem. Phys.* 129:174106
12. Rebentrost P, Mohseni M, Aspuru-Guzik A. 2009. *J. Phys. Chem. B* 113:9942–47
13. Jang S, Cheng YC, Reichman DR, Eaves JD. 2008. *J. Chem. Phys.* 129:101104
14. Jang S. 2009. *J. Chem. Phys.* 131:164101
15. Ishizaki A, Fleming GR. 2009. *J. Chem. Phys.* 130:234110
16. Ishizaki A, Fleming GR. 2009. *J. Chem. Phys.* 130:234111
17. Ishizaki A, Fleming GR. 2009. *Proc. Natl. Acad. Sci. USA* 106:17255–60
18. Palmieri B, Abramavicius D, Mukamel S. 2009. *J. Chem. Phys.* 130:204512
19. Fassioli F, Nazir A, Olaya-Castro A. 2010. *J. Phys. Chem. Lett.* 1:2139–43
20. Nalbach P, Eckel J, Thorwart M. 2010. *N. J. Phys.* 12:065043
21. Thorwart M, Eckel J, Reina JH, Nalbach P, Weiss S. 2009. *Chem. Phys. Lett.* 478:234–37

22. Sarovar M, Ishizaki A, Fleming GR, Whaley KB. 2010. *Nat. Phys.* 6:462–67
23. Ishizaki A, Fleming GR. 2010. *N. J. Phys.* 12:055004
24. Hossein-Nejad H, Scholes GD. 2010. *N. J. Phys.* 12:065045
25. Mukamel S. 2010. *J. Chem. Phys.* 132:241105
26. Olaya-Castro A, Lee CF, Olsen FF, Johnson NF. 2008. *Phys. Rev. B* 78:085115
27. Rebentrost P, Mohseni M, Kassal I, Lloyd S, Aspuru-Guzik A. 2009. *N. J. Phys.* 11:033003
28. Plenio MB, Huelga SF. 2008. *N. J. Phys.* 10:113019
29. Cao J, Silbey RJ. 2009. *J. Phys. Chem. A* 113:13825–38
30. Wu J, Liu F, Shen Y, Cao J, Silbey RJ. 2010. *N. J. Phys.* 12:105012
31. Olbrich C, Strümpfer J, Schulten K, Kleinekathöfer U. 2011. *J. Phys. Chem. B* 115:758–64
32. Olbrich C, Strümpfer J, Schulten K, Kleinekathöfer U. 2011. *J. Phys. Chem. Lett.* 2:1771–76
33. Hoyer S, Sarovar M, Whaley KB. 2010. *N. J. Phys.* 12:065041
34. Sarovar M, Cheng YC, Whaley KB. 2011. *Phys. Rev. E* 83:011906
35. Caruso F, Chin AW, Datta A, Huelga SF, Plenio MB. 2009. *J. Chem. Phys.* 131:105106
36. Caruso F, Chin AW, Datta A, Huelga SF, Plenio MB. 2010. *Phys. Rev. A* 81:062346
37. Fassioli F, Olaya-Castro A. 2010. *N. J. Phys.* 12:085006
38. Scholak T, de Melo F, Wellens T, Mintert F, Buchleitner A. 2011. *Phys. Rev. E* 83:021912
39. Wilde MM, McCracken JM, Mizel A. 2010. *Proc. R. Soc. A* 466:1347–63
40. Brádler K, Wilde MM, Vinjanampathy S, Uskov DB. 2010. *Phys. Rev. A* 82:062310
41. Collini E, Wong CY, Wilk KE, Curmi PMG, Brumer P, Scholes GD. 2010. *Nature* 463:644–48
42. Panitchayangkoon G, Hayes D, Fransted KA, Caram JR, Harel E, et al. 2010. *Proc. Natl. Acad. Sci. USA* 107:12766–70
43. Calhoun TR, Ginsberg NS, Schlau-Cohen GS, Cheng YC, Ballottari M, et al. 2009. *J. Phys. Chem. B* 113:16291–95
44. Ishizaki A, Calhoun TR, Schlau-Cohen GS, Fleming GR. 2010. *Phys. Chem. Chem. Phys.* 12:7319–37
45. Schlau-Cohen GS, Ishizaki A, Fleming GR. 2011. *Chem. Phys.* 386:1–22
46. May V, Kühn O. 2004. *Charge and Energy Transfer Dynamics in Molecular Systems*. Weinheim, Ger.: Wiley-VCH. 2nd ed.
47. Scholes GD. 2003. *Annu. Rev. Phys. Chem.* 54:57–87
48. Renger T. 2009. *Photosynth. Res.* 102:471–85
49. Mukamel S. 1995. *Principles of Nonlinear Optical Spectroscopy.* New York: Oxford Univ. Press
50. Renger T, May V, Kühn O. 2001. *Phys. Rep.* 343:137–254
51. Kubo R, Toda M, Hashitsume N. 1995. *Statistical Physics II: Nonequilibrium Statistical Mechanics*. New York: Springer-Verlag. 2nd ed.
52. Fleming GR, Cho M. 1996. *Annu. Rev. Phys. Chem.* 47:109–34
53. Förster T. 1948. *Ann. Phys.* 437:55–75
54. Sumi H. 1982. *J. Phys. Soc. Jpn.* 51:1745–62
55. Mukamel S, Rupasov V. 1995. *Chem. Phys. Lett.* 242:17–26
56. Jang S, Jung Y, Silbey RJ. 2002. *Chem. Phys.* 275:319–32
57. Perrin F. 1932. *Ann. Phys. (Paris)* 17:283–314
58. Knox RS. 1996. *Photosynth. Res.* 48:35–39
59. Leegwater JA. 1996. *J. Phys. Chem.* 100:14403–9
60. Leggett AJ, Chakravarty S, Dorsey AT, Fisher MPA, Garg A, Zwerger W. 1987. *Rev. Mod. Phys.* 59:1–85
61. Chandler D. 1998. In *Classical and Quantum Dynamics in Condensed Phase Simulations*, ed. BJ Berne, G Ciccotti, DF Coker, pp. 25–49. Singapore: World Sci.
62. Weiss U. 1999. *Quantum Dissipative Systems*. Singapore: World Sci. 2nd ed.
63. Cho M, Vaswani HM, Brixner T, Stenger J, Fleming GR. 2005. *J. Phys. Chem. B* 109:10542–56
64. Redfield AG. 1957. *IBM J. Res. Develop.* 1:19–31
65. Zhang WM, Meier T, Chernyak V, Mukamel S. 1998. *J. Chem. Phys.* 108:7763–74
66. Yang M, Fleming GR. 2002. *Chem. Phys.* 282:163–80
67. Sumi H. 1999. *J. Phys. Chem. B* 103:252–60
68. Mukai K, Abe S, Sumi H. 1999. *J. Phys. Chem. B* 103:6096–102

69. Scholes GD, Fleming GR. 2000. *J. Phys. Chem. B* 104:1854–68
70. Scholes GD, Jordanides XJ, Fleming GR. 2001. *J. Phys. Chem. B* 105:1640–51
71. Jang S, Newton MD, Silbey RJ. 2004. *Phys. Rev. Lett.* 92:218301
72. van Amerongen H, Valkunas L, van Grondelle R. 2000. *Photosynthetic Excitons*. Singapore: World Sci.
73. Kenkre VM, Knox RS. 1974. *Phys. Rev. B* 9:5279–90
74. Rackovsky S, Silbey R. 1973. *Mol. Phys.* 25:61–72
75. Kimura A, Kakitani T, Yamato T. 2000. *J. Phys. Chem. B* 104:9276–87
76. Tao G, Miller WH. 2010. *J. Phys. Chem. Lett.* 1:891–94
77. Huo P, Coker DF. 2010. *J. Chem. Phys.* 133:184108
78. Prior J, Chin AW, Huelga SF, Plenio MB. 2010. *Phys. Rev. Lett.* 105:050404
79. Breuer HP, Petruccione F. 2002. *The Theory of Open Quantum Systems*. New York: Oxford Univ. Press
80. Kubo R. 1969. *Adv. Chem. Phys.* 15:101–27
81. Takagahara T, Hanamura E, Kubo R. 1977. *J. Phys. Soc. Jpn.* 43:811–16
82. Tanimura Y, Kubo R. 1989. *J. Phys. Soc. Jpn.* 58:101–14
83. Nalbach P, Ishizaki A, Fleming GR, Thorwart M. 2011. *N. J. Phys.* 13:063040
84. Jonas DM. 2003. *Annu. Rev. Phys. Chem.* 54:425–63
85. Nagy A, Prokhorenko V, Miller RJD. 2006. *Curr. Opin. Struct. Biol.* 16:654–63
86. Cho M. 2008. *Chem. Rev.* 108:1331–418
87. Abramavicius D, Palmieri B, Voronine DV, Šanda F, Mukamel S. 2009. *Chem. Rev.* 109:2350–408
88. Ginsberg NS, Cheng YC, Fleming GR. 2009. *Acc. Chem. Res.* 42:1352–63
89. Khalil M, Demirdöven N, Tokmakoff A. 2003. *J. Phys. Chem. A* 107:5258–79
90. Khalil M, Demirdöven N, Tokmakoff A. 2004. *J. Chem. Phys.* 121:362–73
91. Pisliakov AV, Mančal T, Fleming GR. 2006. *J. Chem. Phys.* 124:234505
92. Cheng YC, Fleming GR. 2008. *J. Phys. Chem. A* 112:4254–60
93. Womick JM, Moran AM. 2011. *J. Phys. Chem. B* 115:1347–56
94. Collini E, Scholes GD. 2009. *Science* 323:369–73
95. Cheng YC, Fleming GR. 2009. *Annu. Rev. Phys. Chem.* 60:241–62
96. Li YF, Zhou W, Blankenship RE, Allen JP. 1997. *J. Mol. Biol.* 271:456–71
97. Camara-Artigas A, Blankenship RE, Allen JP. 2003. *Photosynth. Res.* 75:49–55
98. Tronrud D, Wen J, Gay L, Blankenship R. 2009. *Photosynth. Res.* 100:79–87
99. Wen J, Tsukatani Y, Cui W, Zhang H, Gross ML, et al. 2011. *Biochim. Biophys. Acta* 1807:157–64
100. Schmidt am Busch M, Müh F, El-Amine Madjet M, Renger T. 2011. *J. Phys. Chem. Lett.* 2:93–98
101. Savikhin S, Buck DR, Struve WS. 1997. *Chem. Phys.* 223:303–12
102. Savikhin S, Buck DR, Struve WS. 1998. *J. Phys. Chem. B* 102:5556–65
103. Vulto SIE, de Baat MA, Louwe RJW, Permentier HP, Neef T, et al. 1998. *J. Phys. Chem. B* 102:9577–82
104. Vulto SIE, Neerken S, Louwe RJW, de Baat MA, Amesz J, Aartsma TJ. 1998. *J. Phys. Chem. B* 102:10630–35
105. Renger T, May V. 1998. *J. Phys. Chem. A* 102:4381–91
106. Wendling M, Pullerits T, Przyjalgowski MA, Vulto SIE, Aartsma TJ, et al. 2000. *J. Phys. Chem. B* 104:5825–31
107. Wendling M, Przyjalgowski M, Gülen D, Vulto S, Aartsma T, et al. 2002. *Photosynth. Res.* 71:99–123
108. Adolphs J, Renger T. 2006. *Biophys. J.* 91:2778–97
109. Müh F, Madjet MEA, Adolphs J, Abdurahman A, Rabenstein B, et al. 2007. *Proc. Natl. Acad. Sci. USA* 104:16862–67
110. Read EL, Schlau-Cohen GS, Engel GS, Wen J, Blankenship RE, Fleming GR. 2008. *Biophys. J.* 95:847–56
111. Wen J, Zhang H, Gross ML, Blankenship RE. 2009. *Proc. Natl. Acad. Sci. USA* 106:6134–39
112. Prezhdo OV, Rossky PJ. 1998. *Phys. Rev. Lett.* 81:5294–97
113. Zanardi P, Rasetti M. 1997. *Phys. Rev. Lett.* 79:3306–9
114. Lidar DA, Chuang IL, Whaley KB. 1998. *Phys. Rev. Lett.* 81:2594–97
115. Lidar DA, Whaley KB. 2003. In *Irreversible Quantum Dynamics, Vol. 622 Springer Lecture Notes in Physics*, ed. F Benatti, R Floreanini, pp. 83–120. Berlin: Springer

116. Kempe J, Bacon D, Lidar DA, Whaley KB. 2001. *Phys. Rev. A* 63:042307
117. Hennebicq E, Beljonne D, Curutchet C, Scholes GD, Silbey RJ. 2009. *J. Chem. Phys.* 130:214505
118. Liu Z, Yan H, Wang K, Kuang T, Zhang J, et al. 2004. *Nature* 428:287–92
119. Standfuss J, Terwisscha van Scheltinga AC, Lamborghini M, Kühlbrandt W. 2005. *EMBO J.* 24:919–28
120. Novoderezhkin VI, Palacios MA, van Amerongen H, van Grondelle R. 2005. *J. Phys. Chem. B* 109:10493–504
121. Frähmcke JS, Walla PJ. 2006. *Chem. Phys. Lett.* 430:397–403
122. Georgakopoulou S, van der Zwan G, Bassi R, van Grondelle R, van Amerongen H, Croce R. 2007. *Biochemistry* 46:4745–54
123. Schlau-Cohen GS, Calhoun TR, Ginsberg NS, Read EL, Ballottari M, et al. 2009. *J. Phys. Chem. B* 113:15352–63
124. Grover LK. 1997. *Phys. Rev. Lett.* 79:325–28
125. Scholes GD. 2010. *Nat. Phys.* 6:402–3
126. Haken H, Strobl G. 1973. *Z. Phys.* 262:135–48
127. Misra B, Sudarshan ECG. 1977. *J. Math. Phys.* 18:756–63
128. Vedral V. 2002. *Rev. Mod. Phys.* 74:197–234
129. Hill S, Wootters WK. 1997. *Phys. Rev. Lett.* 78:5022
130. Isham CJ. 1995. *Lectures on Quantum Theory: Mathematical and Structural Foundations*. London: Imperial Coll. Press
131. Renger T. 2004. *Phys. Rev. Lett.* 93:188101
132. Mukamel S. 2000. *Annu. Rev. Phys. Chem.* 51:691–729
133. Leggett AJ, Garg A. 1985. *Phys. Rev. Lett.* 54:857–60
134. Ollivier H, Zurek WH. 2001. *Phys. Rev. Lett.* 88:017901
135. Billing GD. 2003. *The Quantum Classical Theory.* New York: Oxford Univ. Press
136. Ishizaki A, Fleming GR. 2011. *J. Phys. Chem. B* 115:6227–33
137. Gaab KM, Bardeen CJ. 2004. *J. Chem. Phys.* 121:7813–20
138. Kelly A, Rhee YM. 2011. *J. Phys. Chem. Lett.* 2:808–12
139. Kapral R, Ciccotti G. 1999. *J. Chem. Phys.* 110:8919–29
140. Schrödinger E. 1944. *What is Life? The Physical Aspect of the Living Cell*. Cambridge: Cambridge Univ. Press
141. van Dijk EMHP, Hernando J, García-López JJ, Crego-Calama M, Reinhoudt DN, et al. 2005. *Phys. Rev. Lett.* 94:078302
142. Gerhardt I, Wrigge G, Zumofen G, Hwang J, Renn A, Sandoghdar V. 2009. *Phys. Rev. A* 79:011402
143. Brinks D, Stefani FD, Kulzer F, Hildner R, Taminiau TH, et al. 2010. *Nature* 465:905–8
144. Hildner R, Brinks D, van Hulst NF. 2011. *Nat. Phys.* 7:172–77
145. Scherer NF, Carlson RJ, Matro A, Du M, Ruggiero AJ, et al. 1991. *J. Chem. Phys.* 95:1487–511
146. Scherer NF, Matro A, Ziegler LD, Du M, Carlson RJ, et al. 1992. *J. Chem. Phys.* 96:4180–94
147. Cina JA. 2008. *Annu. Rev. Phys. Chem.* 59:319–42
148. Ohmori K. 2009. *Annu. Rev. Phys. Chem.* 60:487–511
149. Groot ML, Yu JY, Agarwal R, Norris JR, Fleming GR. 1998. *J. Phys. Chem. B* 102:5923–31
150. Wang H, Song X, Chandler D, Miller WH. 1999. *J. Chem. Phys.* 110:4828–40

Annual Review of Condensed Matter Physics

Volume 3, 2012

Contents

Errata

An online log of corrections to *Annual Review of Condensed Matter Physics* articles may be found at http://conmatphys.annualreviews.org/errata.shtml